Ultrasonics Sonochemistry 101 (2023) 106663

Contents lists available at ScienceDirect

Ultrasonics Sonochemistry

journal homepage: www.elsevier.com/locate/ultson

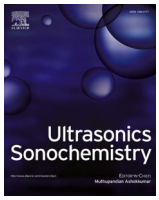

Prediction of shock heating during ultrasound-induced bubble collapse using real-fluid equations of state

Saeed Bidi [a,b,*], Armand Shams [a], Phoevos Koukouvinis [a], Manolis Gavaises [a]

[a] School of Mathematics, Computer Sciences & Engineering, City, University of London, UK
[b] Institut Jean Le Rond D'Alembert, Sorbonne Université and CNRS UMR 7190, F-75005 Paris, France

ARTICLE INFO

Keywords:
Bubble collapse dynamics
Real-liquid EoS
IAPWS data
MNASG
Tait EoS
Shock wave lithotripsy (SWL)

ABSTRACT

Numerical simulations of collapsing air bubbles considering complex and more accurate equations of state (EoS) for estimating the properties of both the liquid and gas are presented. The necessity for utilising such EoSs in bubble collapse simulations is illustrated by the unphysical (spurious) liquid temperature jump formed in the vicinity of the bubble-air interface when simplified EoSs are used. The solved fluid flow equations follow the mechanical equilibrium multiphase method of Kapila. The solver is coded in the AMReX platform, enabling high-performance computation with parallel processing and Adaptive Mesh Refinement for speeding up simulations. It is initially demonstrated that the frequently used Stiffened Gas (SG) EoS overpredicts the liquid temperature at high compression. More sophisticated EoS models, such as the International Association for the Properties of Water and Steam (IAPWS), the Modified Noble Abel Stiffened Gas (MNASG) and a modified Tait EoS introduced here, are also implemented into the flow solver and their differences are highlighted for bubble collapse cases for the first time. Subsequently, application of the developed model to cases of practical interest is showcased. More specifically, simulations of bubble collapse near a solid wall are presented for conditions simulating shock wave lithotripsy (SWL). It is concluded that for such cases, a maximum increase of 25 K of the liquid temperature in contact along the solid wall is caused during the collapse of the air bubble due to shock wave focusing effects. It is also highlighted that the maximum liquid heating varies depending on the initial bubble-wall stand-off distance.

1. Introduction

The bulk liquid temperature does not change significantly compared to that of the bubble content [2–5]. As a result, in the context of thermal effects, attention of the literature is usually directed towards the exceedingly elevated temperature of the contents within the inner bubble, leading to the dissociation of air molecules and triggering chemical reactions. While the surrounding liquid thermodynamics and its impact on the collapse phenomena has not been yet clearly described, the liquid temperature plays a significant role in many applications. Moreover, the liquid thermodynamics determines in high temperature liquids showing an upward trend for both the lifespan and energy of the cavitation bubble [6]. This, however, applies up to a point; beyond that cavitation collapse effects seem to diminish. It is known that the initial liquid temperature affects the bubble dynamics and its lifetime [7–9] as well as the bubble shape stability [10]. The speed and characteristics of cavitation bubble collapses are also influenced by this factor [11]. Liquid thermodynamics sets the kinetic boundary conditions at the interface which can be used to simulate the phase change [12]. It also influences the formation of cavitation-induced pits [13], ultrasonic nanobubbles generation [14], the critical Weber number for forming surface bubbles [15]. Furthermore, modifying the liquid temperature can control the consequences of the bubble collapse. Research indicates that an increased liquid temperature leads to a reduction in the sono-luminescence intensity [16] by reducing the maximum bubble collapse temperature [17]. Another relevant study [18] confirmed this with a different perspective. They stated that liquid can dissolve more gas at lower temperatures. In addition, it was revealed that when water temperatures are lower, the viscosity of the water rises, leading to enhanced stability of the bubble. Consequently, this results in a more intense collapse and amplified sonoluminescence [6]. There are other studies on the impact of the liquid temperature on the sonoluminescence intensities [19,20].

The role of the liquid temperature in cavitation has also been investigated in the industry and more practical applications. For example, experiments show that the cavitation damage to the material is

* Corresponding author.
E-mail address: saeed.bidi@city.ac.uk (S. Bidi).

https://doi.org/10.1016/j.ultsonch.2023.106663
Received 27 September 2023; Accepted 26 October 2023
Available online 2 November 2023

affected by liquid temperature by varying the liquid-jet impact force [21]. A relevant experimental study [22] indicates that mass loss and material removal mechanisms are directly influenced by the liquid temperature in vibratory ultrasonic machining. As a different instance, the primary mechanisms underlying High-Intensity Focused Ultrasound (HIFU) devices involves using cavitation and thermal effects to accurately focus acoustic energy in the body's targeted regions. The main idea is to elevate the temperature above a coagulation threshold rapidly, within a few seconds [23–27] followed by tissue ablation, coagulation, and necrosis through which the tissue will be thermally destroyed while the acoustic energy near the transducer is weak. Applying the HIFU to the targeted area should be carefully controlled in order to keep the rest of the local tissue and skin safe to the greatest extent possible from the thermal and cavitation damage. There are experimental studies on HIFU exposed to tissue-mimicking phantoms or tissues where the temperature increase is measured [28,29]. Part of this temperature rise can be due to ultrasound absorption and conversion to heat while the other part is due to cavitation [6]. Coupling real thermodynamics through applying accurate equations of state with the CFD simulations will aid in modelling the cavitation-enhanced heating which is vital to ensuring safety and analyse the efficiency of the HIFU treatments [28]. As a different application, the role of liquid temperature in erosion is reviewed in [30]. It is argued that the erosion rate initially escalates with rising liquid temperature until a certain threshold, which is between the freezing and boiling points, after which it exhibits a contrary effect. This has been further confirmed by other researchers [11,31,32] where the same temperature dependency was observed for the cavitation impact force.

It should be noted that the surrounding liquid temperature does not remain constant at different collapse stages depending on the settings. For example, it increases during the course of a given HIFU treatment [33]. However, measurement of the temperatures developing during bubble collapse are compromised by the limited spatiotemporal resolution and dynamic range of relevant experimental devices [34]. There have been numerical studies on cavitation where the focus is on the liquid temperature. In some of them, zero-dimensional models have been used to describe the bubble dynamics. In [35], the Keller-Miksis model is used to analyse the spherical bubble collapse energy under ultrasound irradiation. It is demonstrated that the bubble energy slightly increased with the increase in liquid temperature in the range of 283–333 K. In [7], the role of the liquid temperature in bubble dynamics and lifetime was examined by investigating the dependency of the bubble dynamics on the ambient temperature experimentally and comparing the results with the prediction by the modified Rayleigh Plesset model. Shen et al. [36] developed a bubble dynamics model and calculated the liquid temperature at the bubble wall considering the continuity of the energy flux. The liquid temperature at the exterior of the bubble wall was reported up to 1760 K in the case of a strong collapse confirmed by experiments [37]. Peng et al. [38] investigated the influence of liquid temperature on cavitation collapse intensity using the Tait equation of state for water within a zero-dimensional bubble collapse model. They presented a distribution map of the optimum temperature corresponding to the maximum collapse intensity. Shen et al. [39] calculated the spatial distribution of the liquid temperature near a cavitation bubble wall by adopting a bubble dynamics model. They found that the bubble wall preserves the ambient temperature except at strong collapse where heating raises the temperature up to 1510 K.

As zero-dimensional bubble dynamics models cannot simulate non-spherical bubble collapses, CFD methods have been used to model the liquid thermal effects; in the vast majority of relevant studies, the liquid is deemed incompressible and further the Ideal Gas (IG) EoS is utilised. For example, Fursenko et al. [40] simulated a vapor bubble collapse near the microfiber immersed in a subcooled liquid using the Volume of Fluid (VoF) method. Their results indicate that the average jet velocity decreases significantly with an increase of liquid temperature by 50 K. Yu et al. [41] employed an incompressible VoF method coupled with an ideal equation of state to study the thermodynamic effect during bubble collapse near a rigid boundary. In this study, the effects of the formed jet as well as the initial stand-off distance on the bubble thermodynamics are highlighted. In [42], the VoF method was used coupled with the IG EoS to study the collapse of a compressible gaseous bubble surrounded by incompressible water near a heated wall. The findings indicate that an increase in the initial liquid temperature results in the collapse with lower intensity due to a higher vapour pressure inside the bubble. Popinet et al. [43] explored the viscosity's impact on bubble collapse near solid surfaces where reduction of the jet impact velocity at higher viscosity was observed. There are also some relevant studies for cavitation modelling using mass transfer rates [44–48], cavitation modelling using air-vapor–liquid and barotropic EoS [49–53], and heating effects and real-fluid thermodynamic closure in cavitating flows [54–56].

However, the dynamics of bubble rebound are affected by the incompressibility assumption [57], since an important mechanism of energy dissipation as acoustic energy is ignored. Furthermore, since density changes are inherently ignored, an incompressible assumption cannot describe the relevant thermodynamic effects of compression heating [58]. To account for these deficiencies, further CFD studies have progressively been incorporating compressibility effects in bubble collapse simulations. In the majority of them, the Stiffened Gas (SG) EoS [59–64] and Tait [65–71] EoSs have been employed. Although these two EoSs consider liquid compressibility in a straightforward manner, they are unable to describe the liquid thermodynamic behaviour appropriately as the first one uses an unphysical specific heat ratio while the latter does not account for density changes due to temperature variations as explained in Section 2. Therefore, thermal effects were not discussed in these studies. The work of Beig et al. [34] is the most relevant to the present investigation; in this study, a vapour bubble collapse near a solid wall is simulated to quantify the temperature along the wall using the NASG EoS.

The above review shows that simplified thermodynamic assumptions that have been utilised in the vast majority of numerical studies, mainly due to the complexities associated with advanced EoS. It also should be noted that the various EoSs exhibit different accuracy in modelling thermal effects. For instance, in [72] it has been shown that the Gilmore equation for modelling the bubble collapse is used and concluded that the NASG EoS provides a more accurate liquid thermodynamic description than the Tait EoS.

Diffuse Interface Methods (DIM) are widely used for CFD simulation of bubbly flows [73–76] besides the VoF methods [77–80]. Their design aims to calculate flow variables within numerically diffused regions adjacent to interfaces [76]. In the present study, we compare for the first time the predictive capability of a variety of liquid EoSs implemented in the model of Kapila [1] which utilises a DIM. Initially the error introduced by SG EoS is highlighted through a compariso with the International Association for the Properties of Water and Steam (IAPWS) database [82] and also against a newly introduced modified Tait EoS. The lack of accuracy of the SG EoS is plainly presented for a spherical bubble collapse case through a comparison with the results obtained with the Modified Noble Abel Stiffened Gas (MNASG) [83]. Following that, 2D axisymmetric simulations of bubble collapse placed at different stand-off distances from a nearby rigid wall and excited by an ultrasound pressure pulse are performed. In these cases, the MNASG EoS is adopted for approximating the liquid phase properties. It is noted that the real gas thermodynamic model of Redlich-Kwong Peng-Robinson (RKPR) [84], as presented in our earlier work [85], is utilised for approximating the dependence of air bubble content of pressure and temperature. As a result, the liquid temperature elevation along the wall is predicted during the collapse or air bubble placed at different stand-off distances from the wall; such predictions represent one of the main novelties of this research.

The rest of this paper is organised as follows: the various liquid EoSs utilised are compared and their differences are highlighted in Section 2. Following that, in Section 3, the numerical method is presented along with a short description of the AMReX platform [86] where the solver is

developed. Subsequently, the results are demonstrated in Section 4 where the thermal effects in bubble collapse is the focus. Lastly, the concluding remarks are mentioned.

2. Equations of state

The thermodynamic assumptions that affect the materials involved in bubble dynamic cases can play a detrimental role in the temperature distributions and even the dynamics of bubble collapse, although to a much lesser extent. The EoS can play a detrimental role in capturing the aforementioned variations of density during bubble collapse and can shed light on dissipation mechanisms. Further, the formulation of the EoS has a more intrinsic role, as it can affect the predictions of compression heating of the liquid, and thus, consequently influencing the temperature distribution and the heat transfer (from gas to liquid, or from the liquid to nearby solid/soft walls). In fact, in the former work of the authors [85], the relevant EoS has been illustrated to greatly affect compression heating of the bubble contents during strong bubble collapses with the initial pressure ratio (defined as the ratio of external pressure to internal pressure $t = 0$ s) of 353, leading to differences of 4,000 K (or nearly 70 %), between the commonly used IG EoS and real-fluid models. Similar effects, even though to a lesser extent can manifest in the liquid, as it will be further highlighted here. Demonstrating an excellent accuracy and wide range of applicability in our previous work [85], the RKPR EoS is employed in this study for the gas phase in tabulated format with bilinear interpolation as a time-efficient numerical implementation compared to on-the-fly utilisation of the parametric form [87].

2.1. Tait EoS

This is a polytropic-type EoS [88,89] which originally relates liquid pressure to density. The original form of Tait EoS reads as:

$$p = \frac{\rho_0 c_0^2}{n}\left(\left(\frac{\rho}{\rho_0}\right)^n - 1\right) + p_0, \tag{1}$$

where $p, \rho,$ and c are pressure, density and speed of sound, respectively. Subscript 0 denotes the reference state. Moreover, exponent n is set to 7.15 for weakly compressible liquids such as water [90]. Although it is rather simple and accurate in predicting liquid densities, it fails to describe density variations due to temperature and, therefore, compression heating. This is indeed the case for all EoS that links density to pressure only, i.e., having the form $p = f(\rho)$. This observation stems from the fact that, in general, entropy can be written as [91]:

$$ds = \frac{c_p}{T}dT + \frac{1}{\rho^2}\left(\frac{\partial \rho}{\partial T}\right)_p dp. \tag{2}$$

The implication of this equation is that for any EoS written in the form of $p = f(\rho)$, the partial derivative $\left(\frac{\partial \rho}{\partial T}\right)_p$ is zero, hence entropy changes are a function of temperature only. It becomes thus apparent that in such cases, no matter how much a liquid will be compressed in a reversible and adiabatic manner (i.e., isentropic) it will not heat up, and thus the relevant dissipation effects are ignored. The Tait equation of state has been used in improved extensions of the Rayleigh-Plesset equation, such as Keller-Miksis [92] or Gilmore models [72], or resolved 2D/3D bubble dynamic cases [93–95]. Alternative forms that incorporate temperature-related effects have been proposed in the past as discussed in [96], see for example Koop [97] or Saurel [98]; however, in both cases the authors have used a simplified representation for internal energy without considering density variation effects.

While common liquids exhibit weak compressibility, the intense conditions during bubble collapse can lead to significant compressions, reaching magnitudes of many GPa. Furthermore, since in reality the liquid density is affected by temperature also, the aforementioned compression will produce heating of the liquid. On the other hand, the simple liquid EoSs that consider density variations of density due to temperature can greatly overestimate this heating. A particular example of such a model, commonly used in bubble dynamics [99,100], is the SG EoS (for which is the interested reader can refer to the work of Flatten et al. [101] for fundamental thermodynamic relations). To illustrate the deviations that such simplified models can produce, the performance of the simplified and advanced EoSs are compared with the most accurate database IAPWS [82] as a reference formulated in NIST Refprop [102] in the next section.

2.2. Modified Tait EoS

Expressing Eq. (1) for density, an alternative proposed hereafter has the following form:

$$\rho = \left(\frac{p}{\rho_0 c_0^2 f_1(T)} + 1\right)^{1/n} \rho_0 f_2(T), \tag{3}$$

where $f_1(T)$ and $f_2(T)$ are functions that need to be determined. Any candidate formula, as the above, can be fitted to IAPWS datasets using NIST Refprop [102]. Two main parameters are required:

1. The speed of sound should vary with respect to temperature and, at high pressures, decrease with increase of temperature. Here a function in the form of $f_1(T) = \sqrt{\left(\frac{a}{T}\right)}$ was chosen.
2. The isobaric density variation with respect to temperature should have an inflexion point, due to the presence of the critical point. Naturally, this can be expressed by using a sigmoid function, such as *tanh*. Hence, a suitable candidate can have the form:

$$\rho(p,T) = \left(\frac{p}{\rho_0 c_0^2 \sqrt{aT_1/T}} + 1\right)^{1/n} \rho_0 \left[1 - b.\tanh\left(\frac{T - T_1}{T_2}\right)\right]. \tag{4}$$

The selected functions $f_1(T)$ and $f_2(T)$ are produced via data fitting taking numerical stability into account. The incentive behind the general monotonicity is provided in each point, i.e.: (1) speed of sound decreases with respect to temperature and (2) existence of inflection point in density near the critical point. The aforementioned density function defines also the specific volume, $v = \frac{1}{\rho}$. Calibration of this formulation is done using IAPWS database, for a range of 280 −2000 K and 1000 -10^9 Pa. After calibration, the following values for the coefficients are obtained: $T_1 = 650$ K, $T_2 = 550$ K, $a = 0.277096868$, $b = 0.659026$, $\rho_0 = 708.9997$ $\frac{kg}{m^3}$ and $n = 2$. In Fig. 1, red points correspond to IAPWS database, whereas the surface is the plot of the fitted $\rho(p,T)$ function.

Apart from density relation to pressure and temperature, thermodynamic relations for the enthalpy, entropy, speed of sound need to be

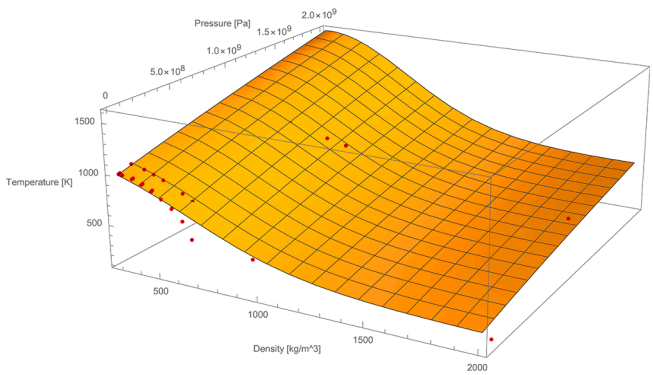

Fig. 1. IAPWS data on the surface plot of $\rho(p,T)$.

defined. For heat capacity at constant pressure there are constraints to be satisfied for the EoS to be consistent. In particular, from the definition of enthalpy $dh = c_p dT + \left(\nu - T\frac{d\nu}{dT}\right)dp$, it has to be an exact differential. Hence, c_p and specific volume are linked, as follows:

$$\frac{dc_p}{dp} = \frac{d}{dT}\left(\nu - T\frac{d\nu}{dT}\right) \Rightarrow c_p = \int_{p_{ref}}^{p} \frac{d}{dT}\left(\nu - T\frac{d\nu}{dT}\right)dp + C_1(T) + C_2. \tag{5}$$

The integral above comes directly from the choice of EoS; the only degree of freedom for adjusting c_p to a reasonable value comes from the functions $C_1(T)$ and C_2, which can be chosen to match experimental data. After fitting, $C_2 = 10334\ \frac{J}{kg.K}$ and $C_1 = -4.889(T-300)$. Also, the enthalpy function can then be obtained by integrating:

$$dh = c_p dT + \left(\nu - T\frac{d\nu}{dT}\right)dp. \tag{6}$$

Similarly, entropy can be obtained by integrating:

$$ds = \frac{c_p}{T}dT + \frac{1}{\rho^2}\frac{d\rho}{dT}dp. \tag{7}$$

Further, various derivatives of density and enthalpy can be defined, once the respective formulation is obtained, as $\frac{dh}{dT}$, $\frac{dh}{dp}$, $\frac{d\rho}{dT}$, and $\frac{d\rho}{dp}$, which can be further used to define speed of sound:

$$c = \sqrt{\frac{\rho\frac{dh}{dT}}{\rho\frac{d\rho}{dp}\frac{dh}{dT} + \frac{d\rho}{dT}\left(1 - \rho\frac{dh}{dp}\right)}}, \tag{8}$$

and heat capacity at constant volume, c_v, as:

$$c_v = c_p - \frac{\left(\frac{1}{v}\frac{dv}{dT}\right)^2}{\left(\frac{1}{\rho}\frac{d\rho}{dp}\right)\rho}. \tag{9}$$

2.3. Noble Abel Stiffened gas (NASG) and MNASG EoSs

The SG EoS involves molecular attractive and agitative forces. The aim of the Noble Abel Stiffened Gas (NASG) is to add repulsive forces to the SG EoS in order to reduce the density error as shown in [103]:

$$p = (\gamma - 1)\frac{(e-q)}{(v-b)} - \gamma p_\infty, \tag{10}$$

where q, p_∞, and b are the fluid heat bond, a characteristic constant, and co-volume as the volume of the molecules' pack, respectively, all depending on the medium. More specifically, the molecular agitation is included in the term $(\gamma-1)(e-q)$ while the repulsive forces are represented by $(v-b)$. The term γp_∞ represents the attractive effects leading to matter cohesion in liquid and solid states. It is noted that setting $q = b = 0$ recovers the original SG EoS. The temperature-based representation of the NASG EoS is derived from the Maxwell rules [103]:

$$T = \frac{(v-b)(p+p_\infty)}{(\gamma-1)c_v}, \tag{11}$$

in which c_v is heat capacity at constant volume. Also, the speed of sound in NASG is obtained from:

$$c^2 = \frac{\gamma v^2(p+p_\infty)}{(v-b)}. \tag{12}$$

The NASG coefficients for liquid water are presented in Table 1.

In [83], it was shown that the NASG EoS overpredicts the water density at low pressures when using the saturation value as the reference state. Therefore, the reference states of the variables were modified to generate new values for p_∞ and b as indicated in Table 2. The resulted thermodynamic closure is the MNASG EoS.

It is noted that a set of $\gamma = 4$, $p_\infty = 6\times10^8$, and $b = q = 0$ converts the above formulae to the common SG EoS for water.

Table 1
NASG coefficients for liquid water.

$c_v\left(\frac{J}{kgK}\right)$	γ	$p_\infty(Pa)$	$b\left(\frac{m^3}{kg}\right)$	$q\left(\frac{J}{kg}\right)$
3610	1.19	7028×10^5	6.61×10^{-4}	−1177788

Table 2
MNASG coefficients for liquid water.

$c_v\left(\frac{J}{kgK}\right)$	γ	$p_\infty(Pa)$	$b\left(\frac{m^3}{kg}\right)$	$q\left(\frac{J}{kg}\right)$
3610	1.19	6217.8×10^5	6.7212×10^{-4}	−1177788

2.4. Comparison of the liquid models

To demonstrate the applicability of the modified Tait EoS both in terms of temperature and density prediction, isentropic compression of liquid water is examined in Fig. 2. The compression starts from 1 bar and 288.15 K. After compression at a given pressure ratio, the water density and temperature increase. As shown below, in the range of calibration the accuracy is rather decent, below 10%, both in terms of temperature and density prediction. In Fig. 3, a similar test is performed with the SG EoS with the same initialisation. As shown, the SG EoS tends to dramatically over-predict the resulting compression heating at high pressures. At a pressure ratio of 10^5, i.e., when liquid is compressed to 10 GPa, the SG EoS predicts a temperature increase of roughly 1282 K. Contrary to this prediction, the IAPWS data predicts a temperature rise of roughly 169 K, almost an order of magnitude lower that the SG prediction. Similarly, a significant error in density prediction of $\approx$ 50% with the SG EoS is observed at this compression ratio.

It becomes apparent that the above can play an important role in research on heat transfer of collapsing bubbles; over/under-prediction of liquid temperature due to the adopted EoS can affect the heat fluxes to or from the bubble. Furthermore, the overestimation of compression heating can be observed even at passing shock waves, emitted during bubble collapses as will be shown in the results section.

Advanced models such as IAPWS come with a larger complexity, which makes them rather cumbersome to implement. Whereas tabulation methods can be applied (see [85,104]) to expedite calculations, their inherent ability to capture phase transitions can cause problems with the numerical solution of the flow equations. Hence, it is of interest to devise robust and versatile thermodynamic closures for liquids, suited for studying bubble collapses.

In the present study, the aforementioned thermodynamic closures, i.e., IAPWS, modified Tait, MNASG, and SG for liquid and RKPR for gas are implemented on a multiphase DIM known as Kapila model outlined in the subsequent section. While MNASG and SG EoSs are applied in their parametric forms, the IAPWS data, modified Tait, and RKPR EoSs are implemented through tabulated format first because of the intricate nature associated with implementation and secondly for faster computation [85]. Each table features a grid with fixed intervals of T and $log_{10}p$ set in a rectangular layout. The temperature and pressure range span $[274, 3000]$ K and $\left[2300, 10^{9.3}\right]$ Pa with 2181 and 745 cells in each direction, respectively, for the IAPWS and modified Tait EoSs. The pressure range is wide enough for low to medium bubble collapse cases up to pressure ratio of $\approx$ 175. For more intense collapses, the MNASG is applied. For the gas phase, the RKPR EoS is applied the temperature and pressure ranges of which are $[60, 17000]$ K and $\left[2300, 1.1\times10^{10}\right]$ Pa with 121 and 375 cells in each direction, respectively.

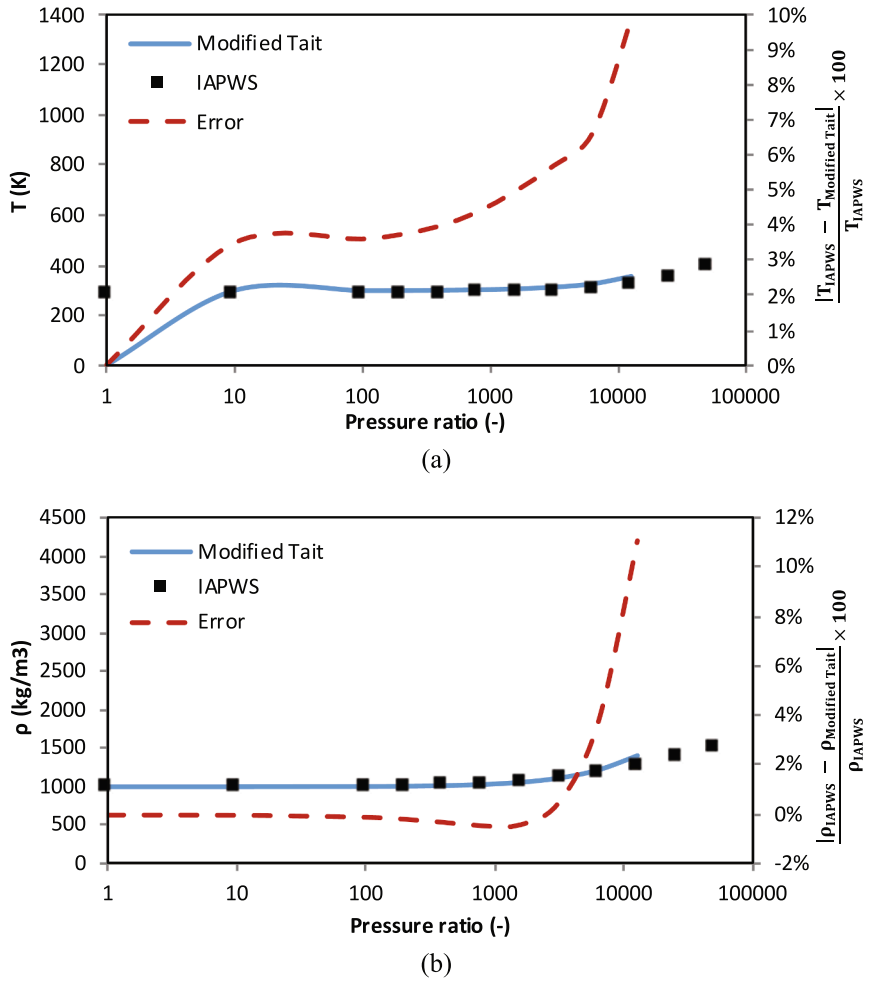

Fig. 2. Comparison of temperature (a) and density (b) obtained with the modified Tait EoS and the IAPWS data at different compression ratios. Squares represent the IAPWS reference, the blue line results of the Modified Tait EoS and the red line is the error in percentage corresponding to the right axis. (For interpretation of the references to colour in this figure legend, the reader is referred to the web version of this article.)

3. Numerical model and methodology

There are many multiphase methods developed for compressible flows in the literature. Those with the least restrictive assumptions consider that the phases are in complete disequilibrium [105,106] indicating that every phase possesses its own velocity, pressure, and temperature. However, due to their complexity, equilibrium assumptions between the co-flowing phases are often considered. In our previous works [85], we expanded the model of [107] which assumes velocity equilibrium but considers pressure and temperature disequilibrium to incorporate tabulated EoSs. There are further models in this context with a variety of equilibrium assumptions [1,75,108,109]. In the present study, the bubble collapse is modelled using a 5-equation mechanical equilibrium multiphase model of Kapila [1], which stems from the full disequilibrium model of Baer-Nunziato [105] assuming zero relaxation time for both velocity and pressure. This model is the most widely used DIM according to [81] for the simulation of compressible two-phase flows. It involves a volume fraction equation, mass balance equations for each phase, a mixture momentum equation, and a total energy equation. Neglecting the effects of viscosity, heat conductivity, surface tension, and phase transition, the model in 1D spherical and 2D axisymmetric coordinates (cylindrical coordinates with azimuthal symmetry) reads:

$$\frac{\partial \boldsymbol{q}}{\partial t}+\frac{\partial \boldsymbol{F}}{\partial r}+\frac{\partial \boldsymbol{G}}{\partial z}=\boldsymbol{s}_{nc}(\boldsymbol{q})+\boldsymbol{s}_{g}(\boldsymbol{q}), \tag{13}$$

where:

$$\boldsymbol{q}=\begin{bmatrix}\alpha_1\\ \alpha_1\rho_1\\ \alpha_2\rho_2\\ \rho u\\ \rho w\\ \rho E\end{bmatrix},\boldsymbol{F}=\begin{bmatrix}\alpha_1 u\\ \alpha_1\rho_1 u\\ \alpha_2\rho_2 u\\ \rho u^2+p\\ \rho uw\\ (\rho E+p)u\end{bmatrix},\boldsymbol{G}=\begin{bmatrix}\alpha_1 w\\ \alpha_1\rho_1 w\\ \alpha_2\rho_2 w\\ \rho uw\\ \rho w^2+p\\ (\rho E+p)w\end{bmatrix},$$

$$\boldsymbol{s_{nc}} = \begin{bmatrix} (K+\alpha_1)\left(\frac{\partial u}{\partial r}+\frac{\partial w}{\partial z}\right) \\ 0 \\ 0 \\ 0 \\ 0 \\ 0 \end{bmatrix},$$

$$\boldsymbol{s_g} = -\frac{\beta}{r}\begin{bmatrix} -Ku \\ \alpha_1\rho_1 u \\ \alpha_2\rho_2 u \\ \rho u^2 \\ \rho uw \\ u(\rho E+p) \end{bmatrix},$$

where value of 2 and 1 for the coordinates switching parameter β correspond to the 1D spherical the r-direction and 2D axisymmetric coordinates in the (r,z) directions, respectively. Also, the following notation is adopted: t (time), ρ (density), p (pressure), α(volume fraction), u (r-direction velocity), w (z-direction velocity), E(specific total energy). Moreover, K is defined as:

$$K = \frac{\rho_2 c_2^2 - \rho_1 c_1^2}{\frac{\rho_2 c_2^2}{\alpha_2} + \frac{\rho_1 c_1^2}{\alpha_1}}, \tag{14}$$

which represents the decrease and increase of the gas volume fraction in the cases of compression and rarefaction waves, respectively. Also, c_k is the speed of sound for phase k. The mixture speed of sound c follows Woods relation [110] as follows:

$$\frac{1}{\rho c^2} = \frac{\alpha_1}{\rho_1 c_1^2} + \frac{\alpha_2}{\rho_2 c_2^2}. \tag{15}$$

As the system of Eq. (13) shows, this model assumes immediate velocity and pressure equilibrium between the phases. The system is solved using a finite volume Godunov method [111] with the second-order MUSCL scheme [112] to reconstruct the primitive variables at the cell boundary. Also, the HLLC approximate solver [113] is employed

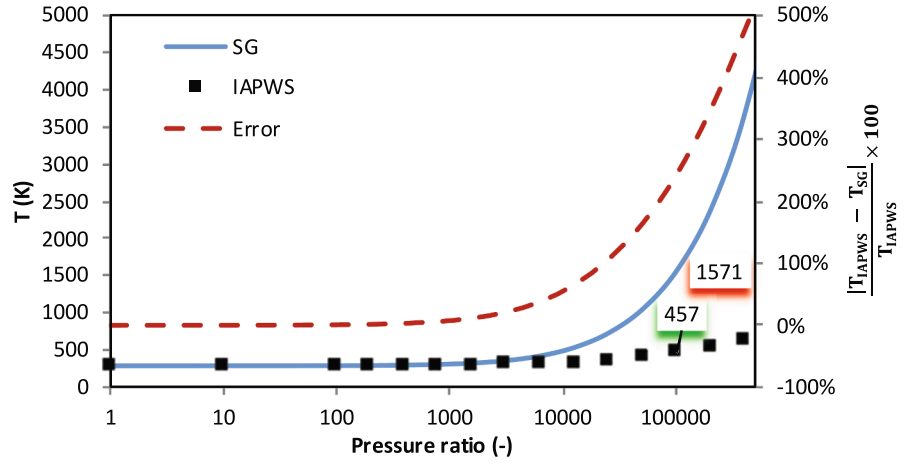

(a)

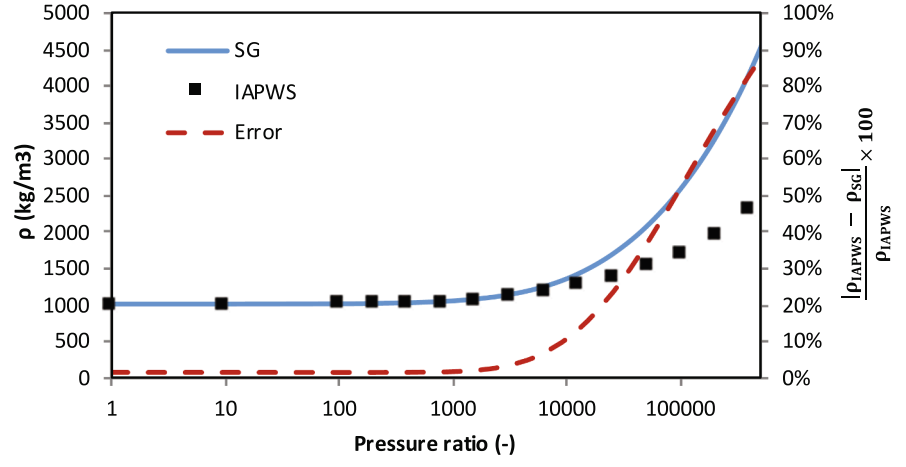

(b)

Fig. 3. Comparison of temperature (a) and density (b) obtained with the SG EoS commonly used in bubble dynamic studies and the IAPWS data at different compression ratios. Squares represent the IAPWS reference, the blue line results of the SG EoS and the red line is the error in percentage corresponding to the right axis. (For interpretation of the references to colour in this figure legend, the reader is referred to the web version of this article.)

for solving the Riemann problem at each cell boundary. The traditional Godunov scheme for updating the conservative component of the system is as follows:

$$\begin{aligned}\boldsymbol{U}_{i,j}^{n+1} = \boldsymbol{U}_{i,j}^{n} - \frac{\Delta t}{\Delta r}\left(\boldsymbol{F}_{cons}^{*}\left(\boldsymbol{U}_{i,j}^{n}, \boldsymbol{U}_{i+1,j}^{n}\right) - \boldsymbol{F}_{cons}^{*}\left(\boldsymbol{U}_{i-1,j}^{n}, \boldsymbol{U}_{i,j}^{n}\right)\right) \\ - \frac{\Delta t}{\Delta z}\left(\boldsymbol{G}_{cons}^{*}\left(\boldsymbol{U}_{i,j}^{n}, \boldsymbol{U}_{i,j+1}^{n}\right) - \boldsymbol{G}_{cons}^{*}\left(\boldsymbol{U}_{i,j-1}^{n}, \boldsymbol{U}_{i,j}^{n}\right)\right) + \Delta t \boldsymbol{s}_{g,cons},\end{aligned} \tag{16}$$

in which:

$$\boldsymbol{U} = \begin{bmatrix} \alpha_1\rho_1 \\ \alpha_2\rho_2 \\ \rho u \\ \rho w \\ \rho E \end{bmatrix}^T, \boldsymbol{F}_{cons} = \begin{bmatrix} \alpha_1\rho_1 u \\ \alpha_2\rho_2 u \\ \rho u^2 + p \\ \rho uw \\ (\rho E + p)u \end{bmatrix}^T, \boldsymbol{G}_{cons} = \begin{bmatrix} \alpha_1\rho_1 w \\ \alpha_2\rho_2 w \\ \rho uw \\ \rho w^2 + p \\ (\rho E + p)w \end{bmatrix}^T,$$

$$\boldsymbol{s}_{g,cons} = -\frac{\beta}{r}\begin{bmatrix} \alpha_1\rho_1 u \\ \alpha_2\rho_2 u \\ \rho u^2 \\ \rho uw \\ u(\rho E + p) \end{bmatrix}^T.$$

The finite volume cell index in (r, z) direction is represented by (i, j) while superscript n indicates the time step. The perturbated state is represented by superscript'*'. Calculation of $\boldsymbol{F}_{cons}^{*}$ and $\boldsymbol{G}_{cons}^{*}$ using the HLLC Riemann solver is discussed in [107]. The volume integral is approximated using a midpoint rule and the divergences with a centered scheme [107] for the non-conservative component:

$$\begin{aligned}\alpha_{i,j}^{n+1} = \alpha_{i,j}^{n} - \frac{\Delta t}{\Delta r}\left((u\alpha)_{i+\frac{1}{2},j}^{*} - (u\alpha)_{i-\frac{1}{2},j}^{*} - \left(\alpha_{i,j}^{n} + K\right)\left(u_{i+\frac{1}{2},j}^{*} - u_{i-\frac{1}{2},j}^{*}\right)\right) \\ - \frac{\Delta t}{\Delta z}\left((w\alpha)_{i,j+\frac{1}{2}}^{*} - (w\alpha)_{i,j-\frac{1}{2}}^{*} - \left(\alpha_{i,j}^{n} + K\right)\left(w_{i,j+\frac{1}{2}}^{*} - w_{i,j-\frac{1}{2}}^{*}\right)\right) + \Delta t\frac{\beta K u}{r}.\end{aligned} \tag{17}$$

At each stage, the mixture pressure is computed using the mixture rule for the internal energy e through the following steps:

$$e = Y_1 e_1 + Y_2 e_2, \tag{18}$$

where $Y_k = \frac{\alpha_k\rho_k}{\rho}$ is the mass fraction for phase k and the phasic internal energies e_k are inserted as functions of pressure and temperature $e_k = e_k(p, T_k)$ through either tabulated data or the analytical relations in the case of the parametric equations of state. The procedure is summarized as follows:

The mixture internal energy e is calculated from the total and kinetic energies:

$$e = E - \frac{1}{2}\left(u^2 + w^2\right). \tag{19}$$

The mixture rule for the internal energies is considered as:

$$e = Y_1 e_1 + Y_2 e_2, \tag{20}$$

where $Y_k = \frac{\alpha_k\rho_k}{\rho}$ and e_k are the mass fraction and phasic internal energy for phase k. In the case of using parametric equations of state for both phases the e_1 and e_2 are inserted as functions of pressure and densities $e_k = e_k(p, \rho_k)$ based on the equations of state such that the pressure will be the only unknown. For instance, in the case of the NASG EoSs, Eq. (20) reads:

$$p = \frac{\rho e - \left(\frac{\alpha_1(1-\rho_1 b_1)\gamma_1 p_{\infty,1}}{\gamma_1 - 1} + \frac{\alpha_2(1-\rho_2 b_2)\gamma_2 p_{\infty,2}}{\gamma_2 - 1}\right) - (\alpha_1\rho_1 q_1 + \alpha_2\rho_2 q_2)}{\frac{\alpha_1(1-\rho_1 b_1)}{\gamma_1 - 1} + \frac{\alpha_2(1-\rho_2 b_2)}{\gamma_2 - 1}}. \tag{21}$$

However, for the more complex equations of state, tabulated or parametric, there is no analytical solution of Eq. (20). Therefore, an iterative method is proposed by defining an error function based on Eq. (19):

$$\epsilon = e - E + \frac{1}{2}\left(u^2 + w^2\right). \tag{22}$$

Newton's method for pressure is used as:

$$p^{(n+1)} = p^{n} - \left(\frac{\epsilon}{\epsilon_p^{'}}\right)^{n}, \tag{23}$$

where $\epsilon_p^{'}$ is the derivative of the error function with respect to the pressure at constant density estimated as:

$$\epsilon_p^{'} = \frac{\Delta\epsilon}{\Delta p} = \frac{e(p + \Delta p) - e(p)}{\Delta p}, \tag{24}$$

where Δp represents a small change in pressure and can be estimated based on the pressure from the previous loop $\Delta p = \xi_p p$ for which $\xi_p = 10^{-3}$ is recommended. Moreover, the initial guess values are considered based on the previous time step. Also, an under-relaxation treatment is also considered to ensure stability. The pressure value is accepted once the solution converges $\left|\frac{\left(p^{(n+1)} - p^{n}\right)}{p^{(n+1)}}\right| < \varepsilon$ with a suggested value of $\varepsilon = 10^{-3}$.

3.1. AMReX implementation

In the present work, the Kapila model with advanced thermodynamics has been implemented in the open source package AMReX [86]; this offers parallel Adaptive Mesh Refinement (AMR) data structures and linear solvers designed for building massively scalable block-structured AMR applications. The platform provides C++ and Fortran interfaces and supports multidimensional systems with parallelisation via MPI or OpenMP (or hybrid) on High Performance Computing (HPC) architectures. It also contains various tools for solving PDEs on structured grids. The first level grid (the coarsest) is generated at the beginning of the simulation, covering the entire domain. Subsequently, the refined levels are built and dynamically change during the simulation depending on selected refinement criteria. In this context, we employ a density gradient approach, characterised by a minimum gradient threshold denoted as $\nabla\rho_{min}$, to guide the refinement process. Whenever the density gradient between adjacent cells exceeds this specified threshold, an additional grid level is generated. It is important to note that this assessment is performed at intervals of every n_{AMR} time steps. This criterion plays a pivotal role in our strategy, serving to both enhance the resolution of interfaces, mitigating diffusion, and optimising computational efficiency by utilising coarser grids in regions exhibiting lower density gradients. Our analysis showed that values of $\nabla\rho_{min} = 1kg/m^3$ and $n_{AMR} = 5$ lead to an efficient computation. To gain insight into the functioning of block-structured Adaptive Mesh Refinement techniques, Fig. 4 illustrates the multilevel refinement approach showcasing three distinct refinement levels at a time step during the non-spherical collapse which will be elaborated in the next section. The AMReX library has been extensively documented in [86,114] and employed for CFD simulations e.g., see [115–117].

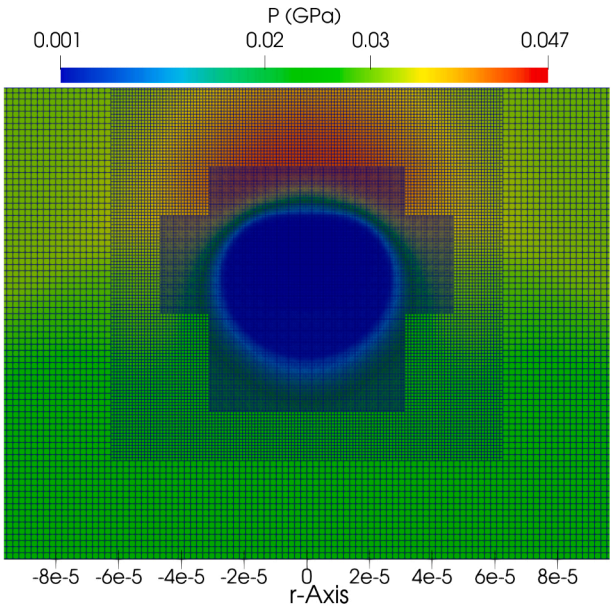

Fig. 4. Block-structured grid with 3 levels of refinement.

4. Results

In this section, we initially investigate the role of the EoS for a pure water shock tube test case. Following that, a spherical bubble collapse is simulated and the results are compared with our previous work [85] employing the relaxation model. Both bubble hydrodynamics and thermodynamics align perfectly, demonstrating the validity of the implementation of the developed tabulated EoS. Subsequently, the effect of the liquid EoS on the spherical bubble collapse is investigated for different pressure ratios. Lastly, a 2D non-spherical collapse is simulated for which the liquid temperature variation along the wall varying with the initial stand-off distance is reported.

In all simulations, three levels of grid refinement are considered, which lead to the grid-independent results. Moreover, there is a minimum volume fraction α_{min} of each phase in the entire domain in the initial setups to ensure the hyperbolicity of the system. Moreover, the monotonized central slop limiter is used for the MUSCL reconstruction scheme, as explained in [107]. The time step varies based on the CFL number which is set to 0.5. Moreover, it is assumed that the bubble is solely filled with air; the initial interior pressure p_{air} is uniform, whereas in the pressure of the water surrounding the bubble follows the distribution described in [118]:

$$p_{water}(r) = p_f + \frac{R_0}{r}\left(p_{air} - p_f\right), \tag{25}$$

where p_f denotes the far-field pressure.

4.1. 1D shock tube

Shock tube problems serve as benchmark tests for the predictive capability of EoSs. Herein, a 3 m long pure water shock tube case has been considered as described in [83]. The diaphragm is placed at $x = 2$ m. Initially, uniform temperature of 300 K prevails while $p = 10^9$ Pa in $x < 2$ m and $p = 10^5$ Pa in $x \geq 2$ m. Velocity starts at zero throughout the domain. The discretisation accounts for a set number of $1,000$ cells, which has been found in prior studies to be sufficient [107]. As discerned from Fig. 5, the SG EoS exhibits a notable temperature jump numerically near the density discontinuity. It is also observed that the results derived from utilising the MNASG EoS align with findings reported in [83]. The SG and

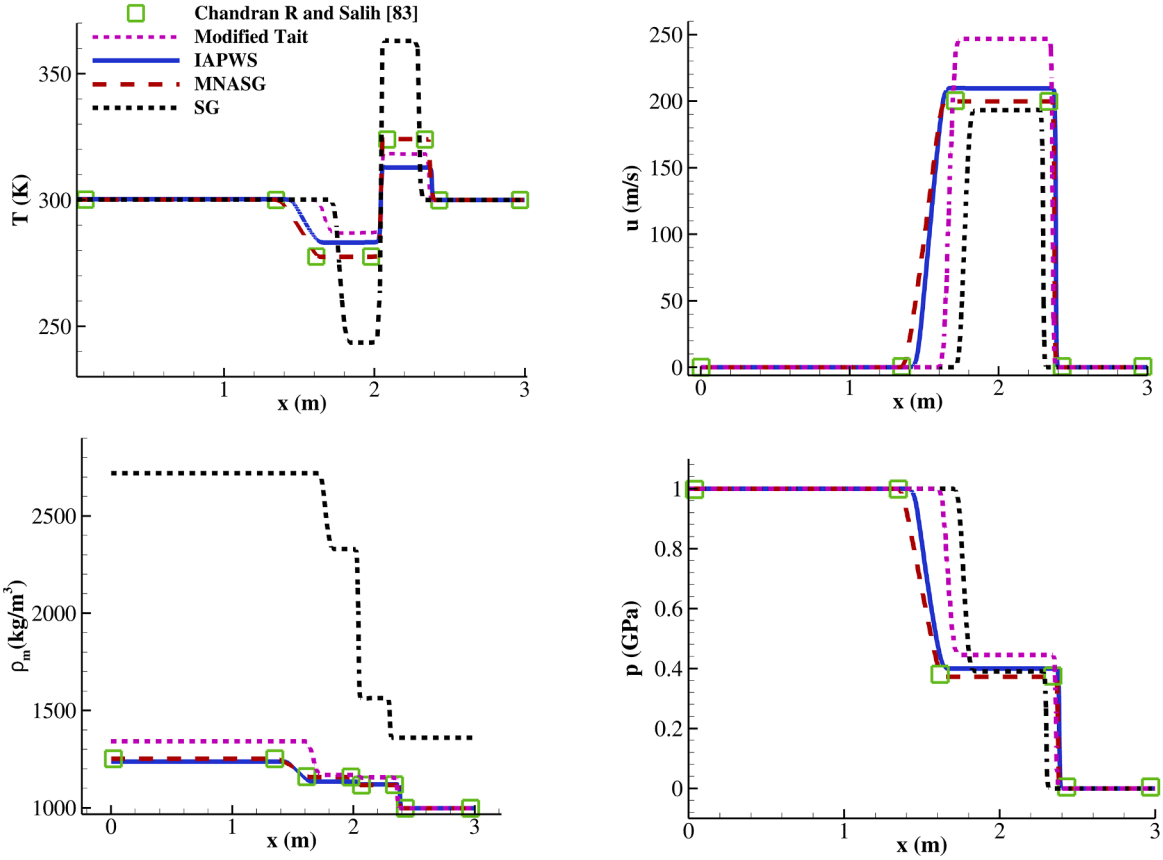

Fig. 5. Water shock tube profile after 200μs with various liquid EoSs for water compared with reference [83].

the modified Tait EoSs lead to the maximum 16% and minimum 1% temperature overpredictions, respectively, relative to the highly precise IAPWS EoS. This is consistent with the findings as outlined in Section 2. It is further noticed that the developed modified Tait EoS has a limited valid range compared to the MNASG for the bubble collapse cases (initial pressure ratio of 180). This might be enhanced in the future by making more astute choices of functions in Eq. (3).

4.2. 1D bubble collapse

The purpose of this test case is twofold; firstly, to validate the solver against widely used bubble collapse cases and secondly, to compare the results against those reported in [85]. More specifically, an 1D spherical bubble with $R_0 = 1$ mm is forced to collapse under the influence of a pressure gradient. The case set up is as follows: $p_{air} = 1.01325 \times 10^5$ Pa, $\rho_{air} = 1.225 \frac{kg}{m^3}$, $p_f = 3.57589 \times 10^7$ Pa, $\rho_{water} = 998.2 \frac{kg}{m^3}$ is set up. The domain length is $L_0 = 20$ mm and it has been discretised using $2,000$ uniformly distributed cells. The plotted radius and time are non-dimensionalised with initial radius R_0 and the Rayleigh collapse time, respectively:

$$R^* = \frac{r}{R_0}, \tag{26}$$

$$t^* = \frac{t}{0.915 R_0 \sqrt{\frac{\rho_{water}}{p_f}}}. \tag{27}$$

For comparison purposes, the RKPR and SG EoSs have been selected for the gas and liquid phases, respectively, similarly to our former study [85]. Fig. 6a shows that excellent agreement between the present simulation against the corresponding results obtained with the Keller-Miksis model; in the latter, the IG EoS is used for the gas phase. This agreement is expected since it is known that the gas EoS has a minimal influence on the change of bubble radius during the collapse [85]. Moreover, the collapse dynamics and the space-averaged bubble temperature are identical to those reported in [85]; it is noted that in this study, a different diffused interface model known as the 'six-equation model' is used with the same equations of state, i.e., the pair of the RKPR and SG EoSs.

After presenting the aforementioned benchmark cases, demonstration of the relative errors that can result from the SG EoS will be reported. In this regard, the initialisation of the previous case is slightly modified by replacing the liquid density with its temperature and lowering the initial pressure ratio as shown in Table 3. This simulation is performed with RKPR EoS for the gas and with the SG, IAPWS, and MNASG EoSs for the liquid phase. Predictions for the temperature in the vicinity of the bubble interface are illustrated in Fig. 7b. It is observed that the SG EoS results in up to 30% temperature overprediction compared to the IAPWS EoS, while the maximum overprediction from

Table 3
Initial conditions for the collapse case with real thermodynamics.

p_{air}(Pa)	p_f(Pa)	$\rho_{air}\left(\frac{kg}{m^3}\right)$	T_{water}(K)
10^5	8.7×10^6	1.225	288

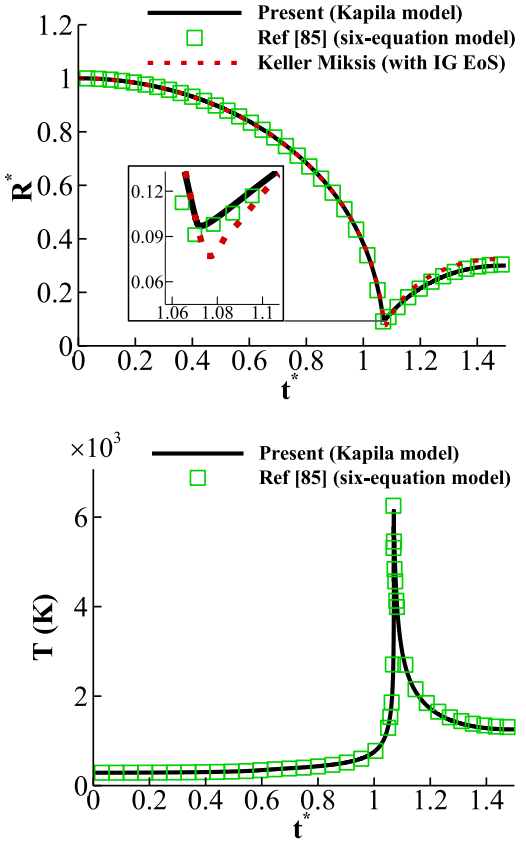

Fig. 6. Comparison of the bubble dynamics (a) and temperature (b) obtained with Kapila model in the present study to the ones with the six-equation model in [85].

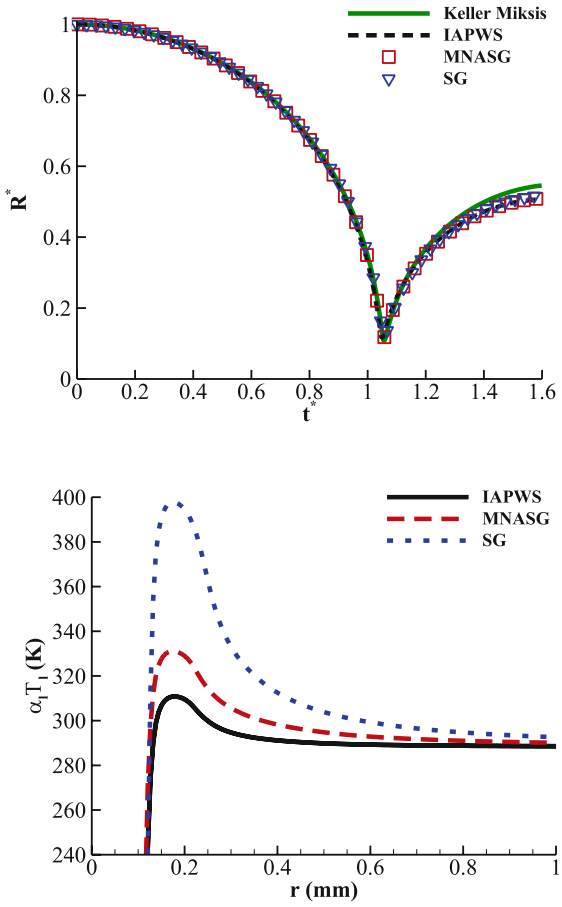

Fig. 7. (a) Bubble dynamics and (b) water temperature predicted by the IAPWS and MNASG EoSs.

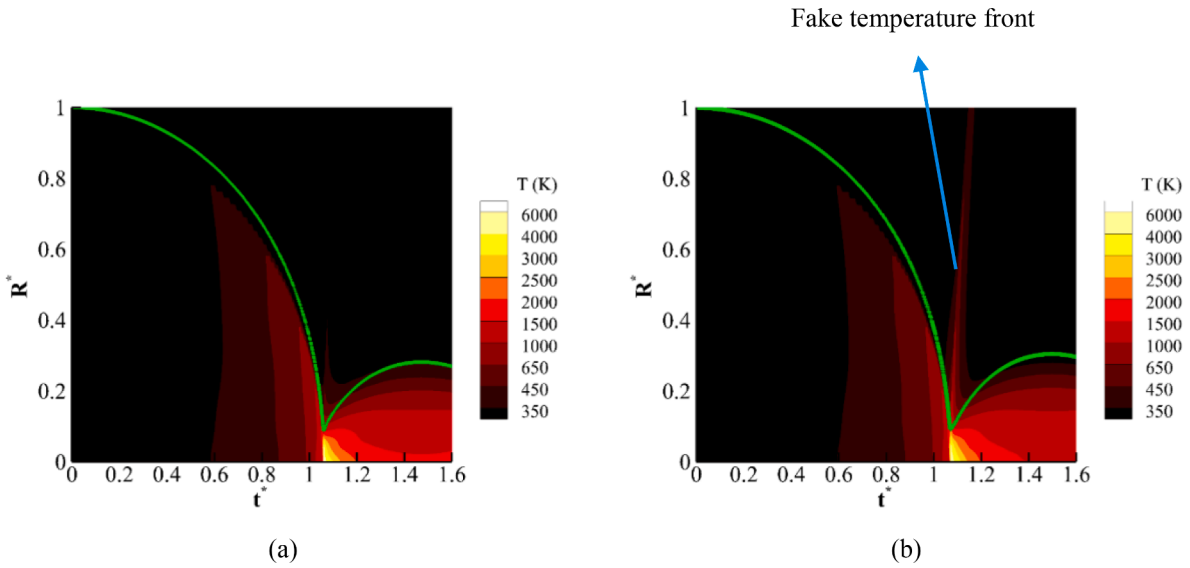

Fig. 8. Spatio-temporal change of the mixture temperature with RKPR EoS for air; and a) MNASG and b) SG EoS for water.

the MNASG EoS is below 6%. It is noteworthy to mention that the original version of the NASG EoS could not accurately depict the dynamics of the collapse.

Since the IAPWS and the modified Tait fail at higher compressions, a stronger collapse with the initial $p_f = 3.57589 \times 10^7$ Pa is simulated here using the MNASG and SG EoSs. The rest of initialisation parameters are the same as in Table 3. It is noted again that the gas EoS is RKPR. The spatio-temporal change of the gas–liquid mixture temperature approximated by $T = Y_g T_g + Y_l T_l$ EoSs is plotted when using MNASG EoS in Fig. 8a and SG EoS in Fig. 8b. The occurrence of a fake temperature front is much more evident when the SG EoS with the maximum of ≈ 700 K while it is much less ≈ 450 K when using MNASG EoS. This indicates that the SG EoS overpredicts a travelling heat wave. It can be also observed that as this will temperature decreases both with time after the collapse point and space move towards the far-field.

4.3. Axisymmetric collapse

One of the diverse applications of ultrasound cavitation in biomedicine is shock wave lithotripsy (SWL). The mechanism of lithotripsy involves producing short focused microsecond pulses that cause shockwave penetrating the body at a target site. During a treatment session,

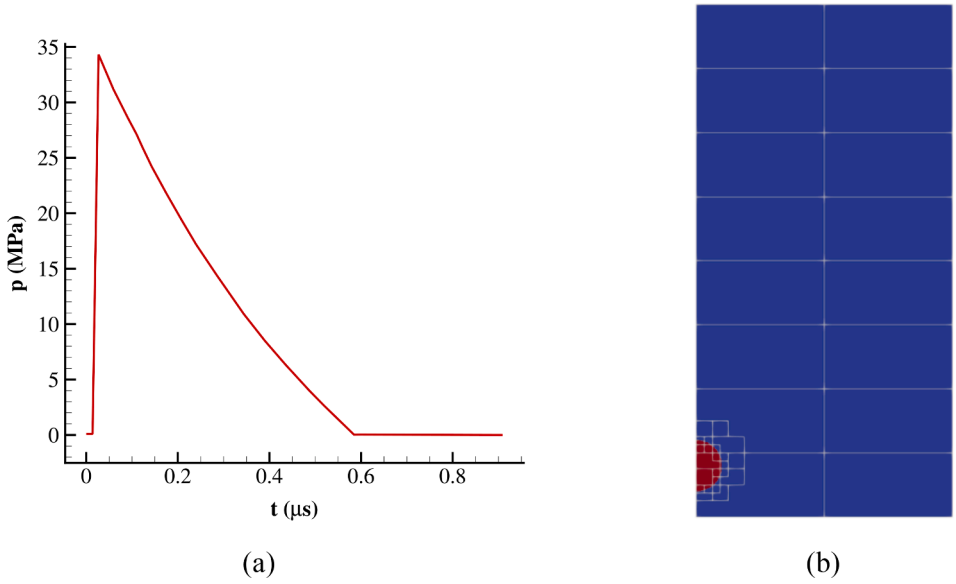

Fig. 9. (a) Pressure pulse of the lithotripter and (b) Schematic of the initial setup for the non-spherical collapse case with block structured grid in AMReX.

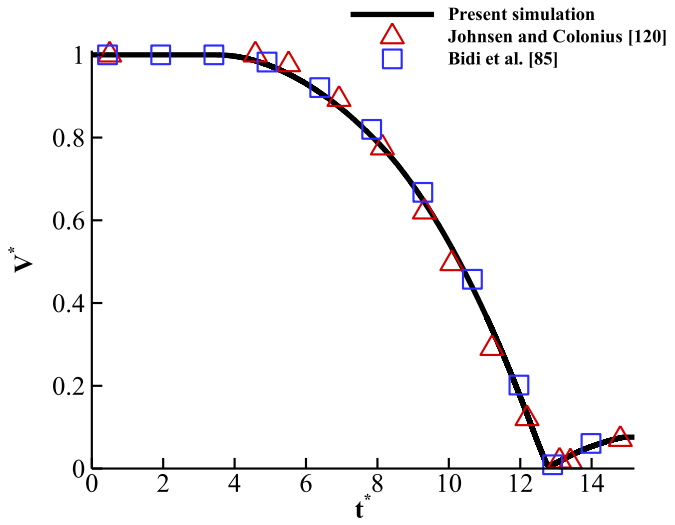

Fig. 10. Bubble dynamics of shock-induced collapsing bubble using RKPR and MNASG EoSs compared with [85,120].

numerous pulses are administered, typically at frequencies ranging between 1 and 2 Hz. Cavitation is known to affect both the intended fragmentation of stones and the unintended harm to surrounding tissues [119]. While increasing the pulse rates could expedite the treatment process, it could also lead to tissue damage [119,24].

A simplified representation for SWL can be examined as follows. A compressive shock front from the upper boundary depicted in Fig. 9a represents the lithotripter pulse without the tensile part propagating in time; this is based on an analytical function described in [120] resembling that of an electrohydraulic lithotripter system Dornier HM3, which is a commonly used lithotripter. This test case was first introduced in the work of [120], where they studied the wall pressure subjected to the bubble collapse. In this setup, infinite impedance for the kidney stone is assumed to avoid any wave absorption in the boundary.

Initially, the pressure is atmospheric in the whole computational domain; the water and air densities are $\rho_{water} = 998.2\,kg/m^3$ and $\rho_{air} = 1.125\,kg/m^3$, respectively. To reduce the computational cost, the case is simulated in 2D axisymmetric coordinates instead of the full 3D configuration. The schematic of the geometry is presented in Fig. 9b where the domain is divided into separate blocks while the grid is refined in the proximity of the liquid–air interface. Reflective boundary condition is used on the axis of symmetry whereas for the right side and the bottom wall, the non-reflective and no-slip boundary conditions

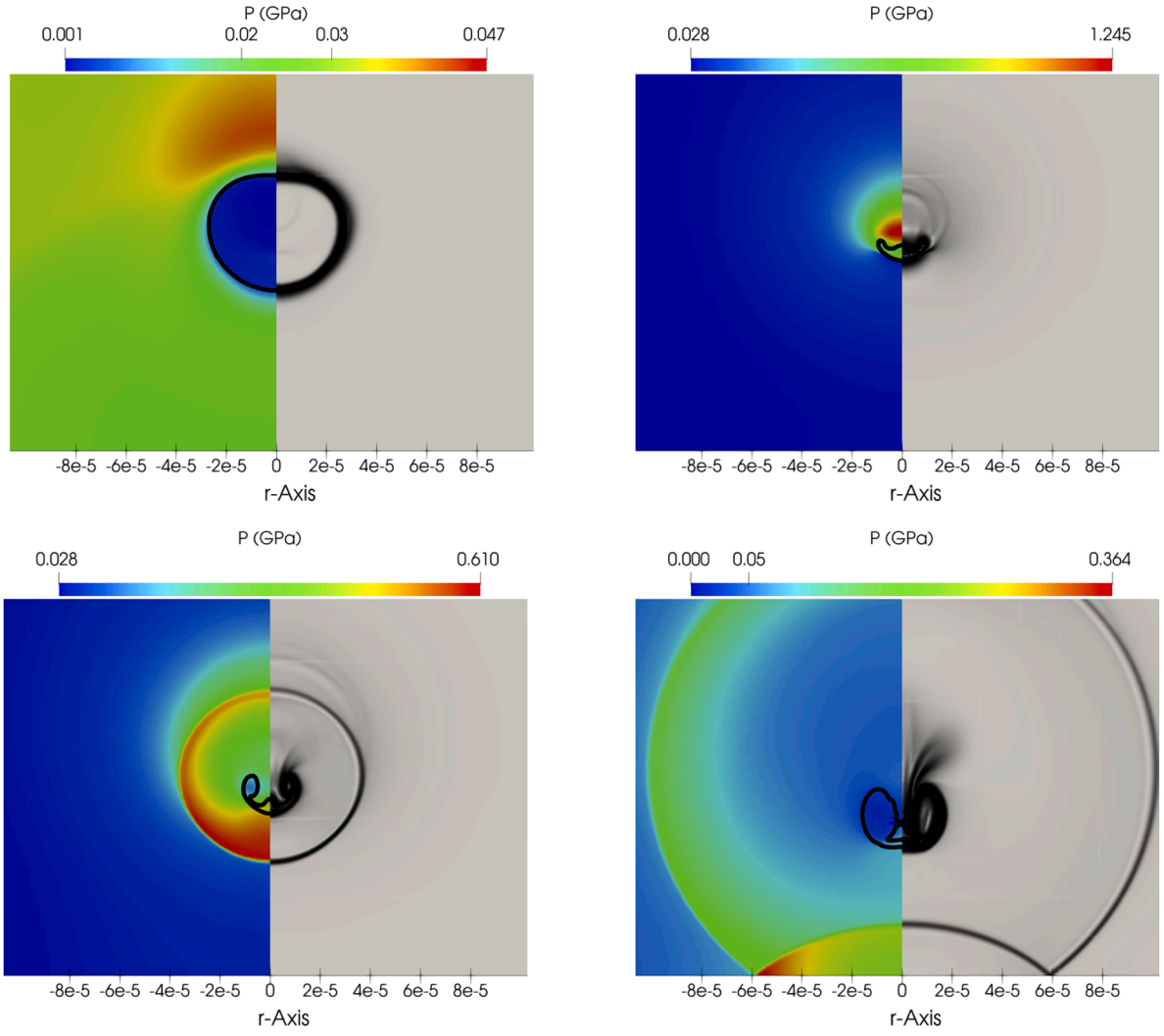

Fig. 11. Pressure field (left half), numerical Schlieren (right half) at different collapse stages: a) $t^* = 11.50$, b) $t^* = 12.65$, c) $t^* = 13.07$, and d) $t^* = 14.41$.

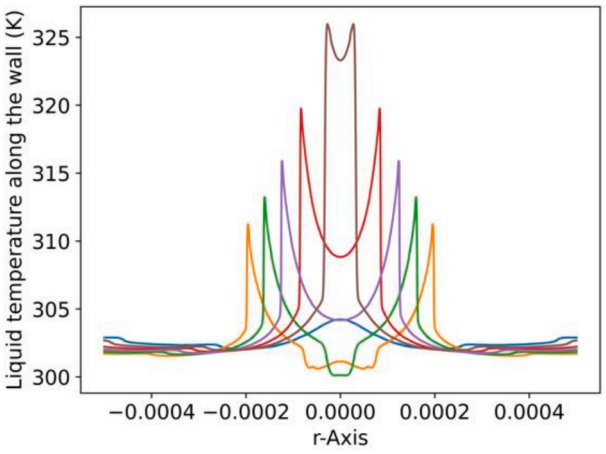

(a)

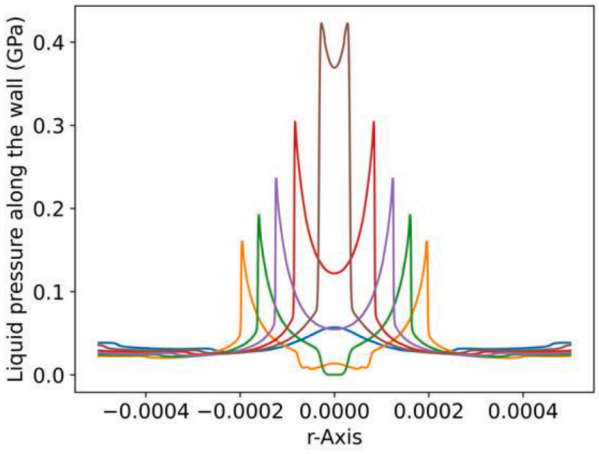

(b)

Fig. 12. Liquid temperature (a) and pressure (b) along the wall at different times after the shock hits the wall.

have been used, respectively. The bubble has an initial radius of $R_0 = 0.05$ mm while the initial stand-off distance, defined as the minimum distance between the bubble centre and the wall, is $H_0 = 2R_0$.

The temporal variation of the bubble volume is initially shown in Fig. 10. For consistency with the results reported in [120], the bubble volume is normalised with its initial value $V^* = V/V_0$ and the time is non-dimensional using $t^* = tc_L/R_0$. In this case, $c_L = 1,647\, m/s$ is the reference speed of sound. The results obtained with the ideal and real gas EoSs are compared with the study of [120]; overall, good agreement is achieved, as expected.

Further details of the collapse process are illustrated in the following plots. More specifically, the relevant pressure and numerical Schlieren contours from various moments during the collapse are showcased in Fig. 11. For these simulations, the MNASG has been utilised as it was found in the previous section to predict the liquid temperature more accurately. The liquid temperature distribution along the wall is illustrated in Fig. 12a within this context. It is evident that temperature remains relatively stable and with no substantial change before the final stage of the collapse. At this point, an increase of 25 K is predicted at the time when the shock wave hits the wall. A similar pattern is observed for pressure in Fig. 12b where the wall pressure exceeds 0.4 GPa.

In order to gain a deeper insight into the dynamic evolution of liquid temperature, temperature contours are presented in Fig. 13; the plotted temperature values are masked to values up to the maximum value in the liquid phase (thus, the much higher temperatures inside the bubble appear as empty). On the right-hand side of the same plots, the contours depicting the magnitude of the velocity field are plotted.

According to Fig. 13b it becomes apparent that the liquid temperature can rise significantly to 340 K in the region above the bubble before the collapse. During the rebound, this region cools down while the liquid temperature in the proximity of the bubble is still high, as shown in Fig. 13c. Subsequently, the shock propagates towards the wall where the liquid temperature along the wall increases to 340 K, as depicted in Fig. 13d. Evidently, the shock wave causes this heating rather than the propagation of the pressure pulse of the lithotripter. To further elaborate on this observation, the impact of the initial bubble stand-off distance from the wall on the subsequent rise of liquid temperature have been studied, using various initial stand-off distances. Fig. 14 highlights the

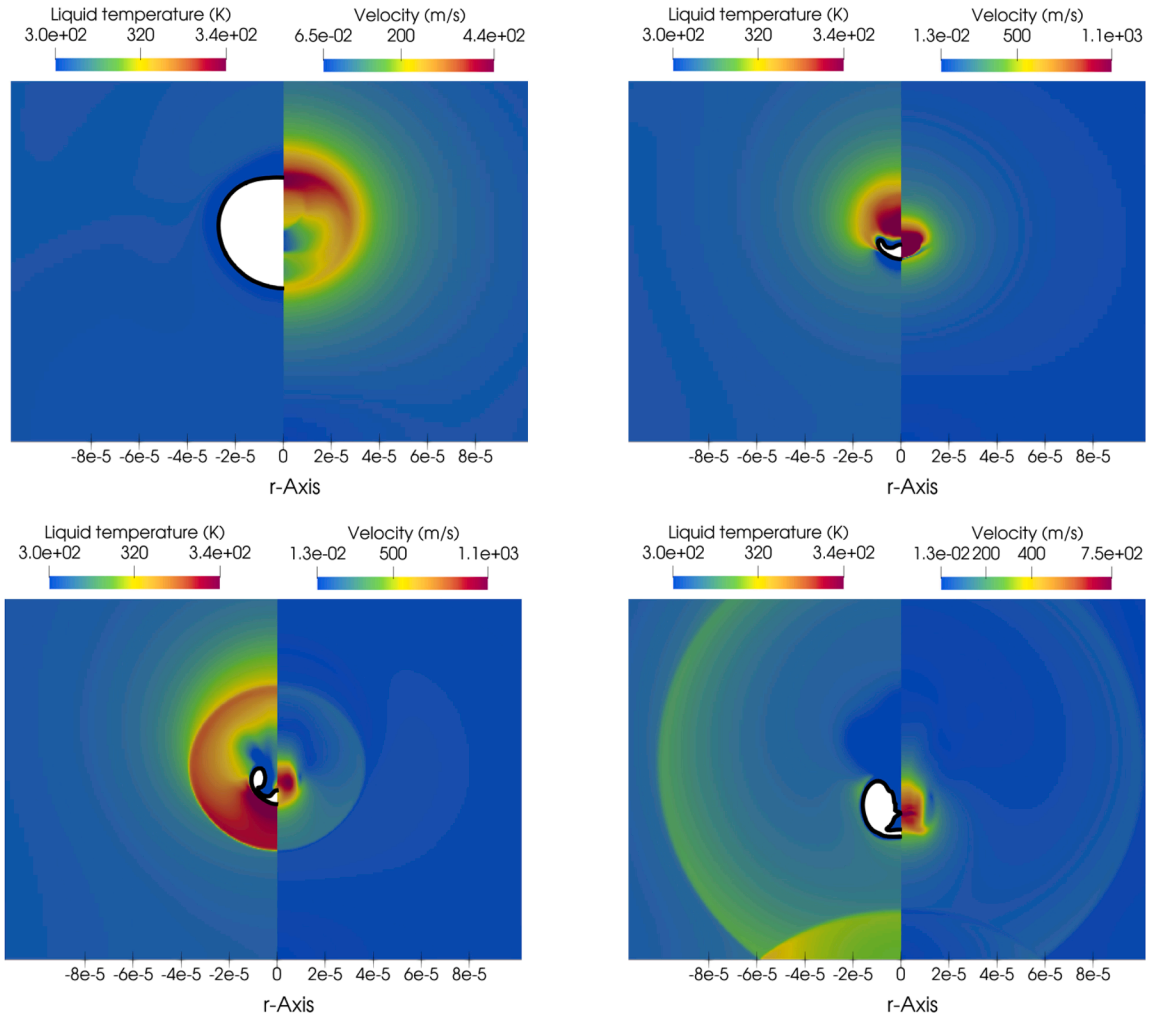

Fig. 13. Liquid temperature (left side) and velocity magnitude (right side) at different collapse stages.

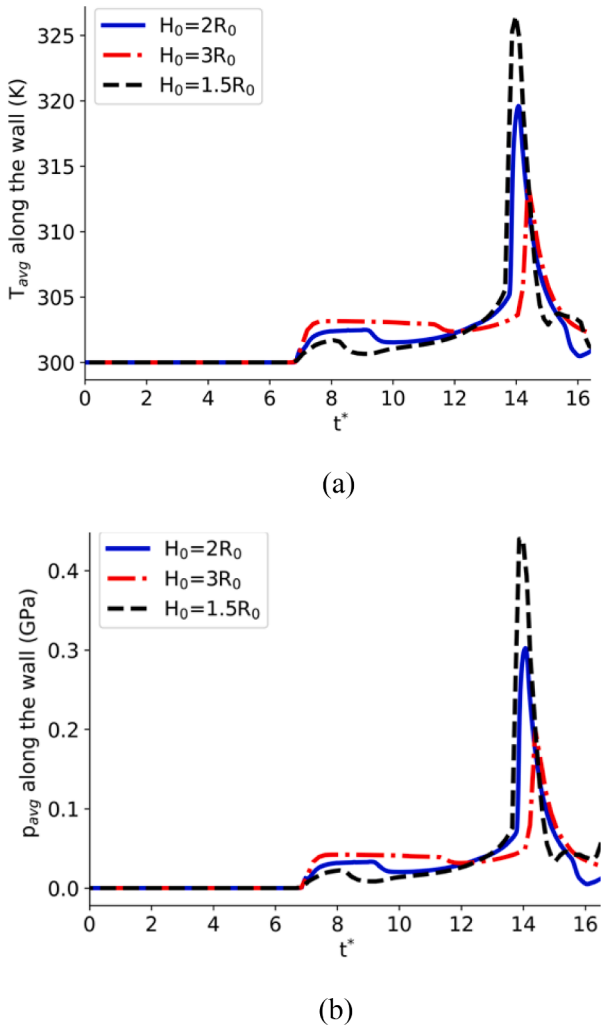

Fig. 14. Spaced-averaged (in $r < R_0$) liquid temperature (a) and pressure (b) along the wall over time.

temporal evolution of the space-averaged liquid temperature and pressure within the region $r < R_0$. As depicted in this figure, a decrease in the initial stand-off distance results in an increase in both the liquid temperature along the wall and the pressure, consistent with the observations reported in [34].

Finally, the heatmap of the temporal change of the liquid temperature along the rigid wall is depicted in Fig. 15 where the horizontal axis shows the time while the vertical axis represents the rigid wall axis. Accordingly, it is observed that the temperature increase due to the pressure pulse is not significant. However, as the bubble collapses, the maximum temperature raise to $T = 325$ K below the bubble in $r \approx (0, 0.02)$ mm while tissue damage occurs usually above 325 K [121]. As time progresses, the region exhibiting the highest temperature gradually migrates towards the right boundary, with a reduction in its magnitude.

5. Conclusion

In the current study, we expand the Kapila model to incorporate complex EoSs for both the liquid and gas phases. Since real gas effects during bubble collapses were extensively discussed in our former work, the present work has focused on the thermal effects induced in the liquid phase. Particularly, the deficiencies of EoS for the liquid state ought to both the unphysical specific heat ratio and the absence of terms considering repulsive molecular effects was showcased. It was observed that the SG EoS leads to above 800% error in temperature rise compared to the prediction obtained with the IAPWS one, at the highest compression of 10 GPa investigated. Moreover, the more complex and accurate modified Tait and IAPWS EoS were able to resolve and eliminate the spurious liquid temperature front that is predicted when the SG EoS was used, and which can be as high as 400 K. Having demonstrated the ability of the proposed liquid EoS to predict the temperature variation for the benchmark bubble collapse cases, the liquid temperature developing along a solid wall exposed to the violent bubble collapse induced by an ultrasonic pressure pulse simulating that of a commercial lithotripter was studied. Model predictions indicated that the temperature increase during a single collapse event is a function of the bubble initial stand-off distance; shorter initial stand-off distance lead to higher liquid temperatures along the wall.

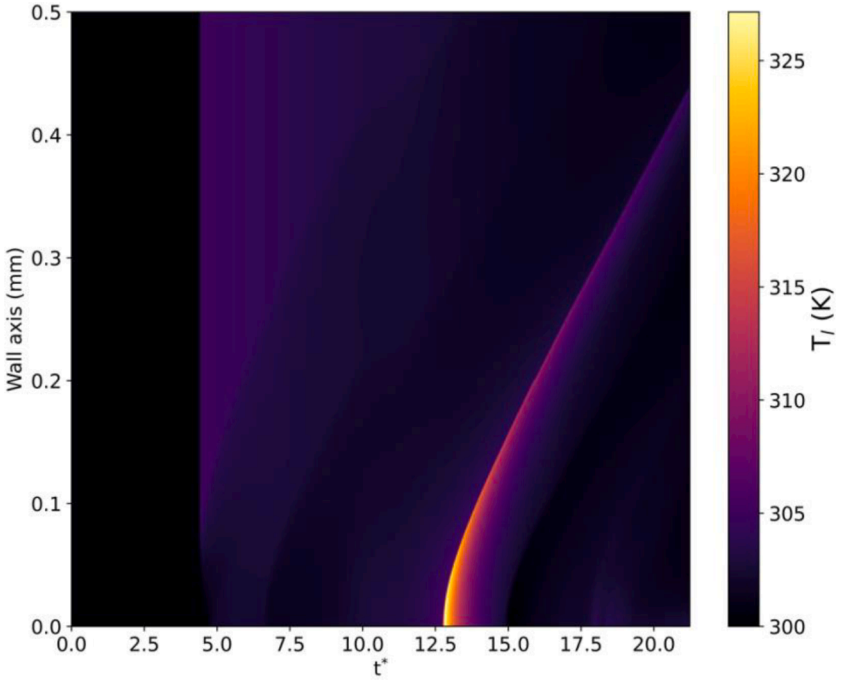

Fig. 15. Spatio-temporal change of the liquid temperature along the wall axis.

Declaration of Competing Interest

The authors declare that they have no known competing financial interests or personal relationships that could have appeared to influence the work reported in this paper.

Data access statement

The Supporting Information is available free of charge on the ACS Publications website at DOI: 10.25383/city.21262635.

Acknowledgments

This work was supported by the European Union Horizon-2020 Research and Innovation Programme (UCOM Project), Grant Agreement No. 813766. Additional funding has been received by the UK's Engineering and Physical Sciences Research Council (EPSRC) through grant EP/K020846/1. The authors express their gratitude to Prof. Stéphane Zaleski for his invaluable support and insightful discussions regarding this study.

Appendix A. Supplementary data

Supplementary data to this article can be found online at https://doi.org/10.1016/j.ultsonch.2023.106663.

References

[1] A.K. Kapila, R. Menikoff, J.B. Bdzil, S.F. Son, D.S. Stewart, Two-phase modeling of deflagration-to-detonation transition in granular materials: reduced equations, Phys. Fluids 13 (10) (2001) 3002–3024, https://doi.org/10.1063/1.1398042.
[2] A. Prosperetti, M.S. Plesset, Vapour-bubble growth in a superheated liquid, J Fluid Mech 85 (2) (1978) 349–368, https://doi.org/10.1017/S0022112078000671.
[3] A. Prosperetti, L.A. Crum, K.W. Commander, Nonlinear bubble dynamics, J. Acoust. Soc. Am. 83 (2) (1988) 502–514, https://doi.org/10.1121/1.396145.
[4] V.K. Prosperetti, A. Prosperetti, A theoretical study of sonoluminescence, Synth Met 76 (1–3) (1993) 213–216, https://doi.org/10.1016/0379-6779(95)03455-S.
[5] Eds. Crum, A. Lawrence, Timothy J. Mason, Jacques L. Reisse, Kenneth S. Suslick, Sonochemistry and Sonoluminescence, Springer Science & Business Media, 1998.
[6] *Cavitation in Biomedicine*. Springer Netherlands, 2015. doi: 10.1007/978-94-017-7255-6.
[7] X. Liu, Y. Hou, X. Liu, J. He, J. Lu, X. Ni, Oscillation characteristics of a laser-induced cavitation bubble in water at different temperatures, Optik (Stuttg) 122 (14) (2011) 1254–1257, https://doi.org/10.1016/j.ijleo.2010.08.010.
[8] T.H. Phan, E. Kadivar, V.T. Nguyen, O. El Moctar, W.G. Park, Thermodynamic effects on single cavitation bubble dynamics under various ambient temperature conditions, Phys. Fluids 34 (2) (2022) pp, https://doi.org/10.1063/5.0076913.
[9] J. Lee, G. Son, A sharp-interface level-set method for compressible bubble growth with phase change, Int. Commun. Heat Mass Transfer 86 (June) (2017) 1–11, https://doi.org/10.1016/j.icheatmasstransfer.2017.05.016.
[10] K. Klapcsik, F. Hegedűs, Study of non-spherical bubble oscillations under acoustic irradiation in viscous liquid, Ultrason Sonochem 54 (2018) (2019) 256–273, https://doi.org/10.1016/j.ultsonch.2019.01.031.
[11] X. Liu, et al., Experimental study of temperature effect on the growth and collapse of cavitation bubbles near a rigid boundary, Optoelectron Lett 9 (4) (2013) 317–320.
[12] M. Kon, K. Kobayashi, M. Watanabe, Liquid temperature dependence of kinetic boundary condition at vapor-liquid interface, Int J Heat Mass Transf 99 (2016) 317–326, https://doi.org/10.1016/j.ijheatmasstransfer.2016.03.088.
[13] N. Takada, T. Nakano, K. Sasaki, Formation of cavitation-induced pits on target surface in liquid-phase laser ablation, Appl Phys A Mater Sci Process 101 (2) (2010) 255–258, https://doi.org/10.1007/s00339-010-5812-z.
[14] J. Il Lee, J.M. Kim, "Influence of temperature on bulk nanobubble generation by ultrasonication", *Colloids and Interface Science*, Communications vol. 49, no. June (2022), 100639, https://doi.org/10.1016/j.colcom.2022.100639.
[15] M.J. Xu, J.Q. Zhang, Q. Li, S.X. Lu, The influence of liquid pool temperature on the critical impact Weber number for surface bubble formation, Int J Heat Mass Transf 127 (2018) 677–682, https://doi.org/10.1016/j.ijheatmasstransfer.2018.08.085.
[16] P. Keshao. Chendke, The sonoluminescence and sonochemical reactions of aqueous solutions, University of Michigan, 1982.
[17] S. Merouani, O. Hamdaoui, Y. Rezgui, M. Guemini, Computer simulation of chemical reactions occurring in collapsing acoustical bubble: Dependence of free radicals production on operational conditions, Res. Chem. Intermed. 41 (2) (2015) 881–897, https://doi.org/10.1007/s11164-013-1240-y.
[18] R. Hiller, S.J. Putterman, B.P. Barber, Spectrum of synchronous picosecond sonoluminescence, Phys Rev Lett 69 (8) (1992) 1182–1184, https://doi.org/10.1103/PhysRevLett.69.1182.
[19] M. Germano, A. Alippi, A. Bettucci, F. Brizi, D. Passeri, Water temperature dependence of single bubble sonoluminescence threshold, Ultrasonics 50 (1) (2010) 81–83, https://doi.org/10.1016/j.ultras.2009.08.007.
[20] A. Moshaii, S. Tajik-Nezhad, M. Faraji, Temperature dependency of single-bubble sonoluminescence in sulfuric acid, Phys Rev E 84 (4) (2011) 46301.
[21] X. Liu, et al., Temperature effect on the impact of a liquid-jet against a rigid boundary, Optik (Stuttg) 124 (13) (2013) 1542–1546, https://doi.org/10.1016/j.ijleo.2012.04.020.
[22] A.P. Nagalingam, S.H. Yeo, Effects of ambient pressure and fluid temperature in ultrasonic cavitation machining, International Journal of Advanced Manufacturing Technology 98 (9–12) (2018) 2883–2894, https://doi.org/10.1007/s00170-018-2481-0.
[23] G.R. Ter Haar, High intensity focused ultrasound for the treatment of tumors, Echocardiography 18 (4) (2001) 317–322.
[24] M.R. Bailey, V.A. Khokhlova, O.A. Sapozhnikov, S.G. Kargl, L.A. Crum, Physical mechanisms of the therapeutic effect of ultrasound (a review), Acoust Phys 49 (2003) 369–388.
[25] J.E. Kennedy, High-intensity focused ultrasound in the treatment of solid tumours, Nat Rev Cancer 5 (4) (Apr. 2005) 321–327, https://doi.org/10.1038/nrc1591.
[26] G. ter Haar, C. Coussios, High intensity focused ultrasound: physical principles and devices, Int. J. Hyperth. 23 (2) (Jan. 2007) 89–104, https://doi.org/10.1080/02656730601186138.
[27] G. ter Haar, Therapeutic applications of ultrasound, Prog Biophys Mol Biol 93 (1–3) (Jan. 2007) 111–129, https://doi.org/10.1016/J.PBIOMOLBIO.2006.07.005.
[28] R.G. Holt, R.A. Roy, Measurements of bubble-enhanced heating from focused, MHz-frequency ultrasound in a tissue-mimicking material, Ultrasound Med Biol 27 (10) (2001) 1399–1412.
[29] D.J. Watmough, et al., The effect of gas bubbles on the production of ultrasound hyperthermia at 0.75 MHz: a phantom study, Ultrasound Med Biol 19 (3) (1993) 231–241.
[30] J.G. Auret, O. Damm, G.J. Wright, F.P.A. Robinson, Cavitation erosion of copper and aluminium in water at elevated temperature, Tribol Int 26 (6) (1993) 421–429.
[31] S. Hattori, A. Nimura, H. Yada, Effect of temperature on cavitation erosion of 9Cr steel in liquid metal, Wear 303 (1–2) (2013) 269–275.
[32] M. Dular, Hydrodynamic cavitation damage in water at elevated temperatures, Wear 346–347 (2016) 78–86, https://doi.org/10.1016/j.wear.2015.11.007.
[33] W. Kreider, M.R. Bailey, O.A. Sapozhnikov, L.A. Crum, Potential temperature limitations of bubble-enhanced heating during HIFU, AIP Conference Proceedings 1215 (2010) 367–370, https://doi.org/10.1063/1.3367182.
[34] S.A. Beig, B. Aboulhasanzadeh, E. Johnsen, Temperatures produced by inertially collapsing bubbles near rigid surfaces, J Fluid Mech 852 (2018) 105–125, https://doi.org/10.1017/jfm.2018.525.
[35] S. Merouani, O. Hamdaoui, Y. Rezgui, M. Guemini, Energy analysis during acoustic bubble oscillations: Relationship between bubble energy and sonochemical parameters, Ultrasonics 54 (1) (2014) 227–232, https://doi.org/10.1016/j.ultras.2013.04.014.
[36] Y. Shen, K. Yasui, T. Zhu, M. Ashokkumar, A model for the effect of bulk liquid viscosity on cavitation bubble dynamics, PCCP 19 (31) (2017) 20635–20640, https://doi.org/10.1039/c7cp03194g.
[37] R.E.C.K.S. Suslick, D.A. Hammerton, The sonochemical hot spot, J Am Chem Soc (1986) 5641–5642.
[38] K. Peng, F.G.F. Qin, R. Jiang, S. Kang, Interpreting the influence of liquid temperature on cavitation collapse intensity through bubble dynamic analysis, Ultrason Sonochem 69 (2020), 105253, https://doi.org/10.1016/j.ultsonch.2020.105253.
[39] Y. Shen, K. Yasui, Z. Sun, B. Mei, M. You, T. Zhu, Study on the spatial distribution of the liquid temperature near a cavitation bubble wall, Ultrason Sonochem 29 (2016) 394–400, https://doi.org/10.1016/j.ultsonch.2015.10.015.
[40] R.V. Fursenko, V.M. Chudnovskii, S.S. Minaev, J. Okajima, Mechanism of high velocity jet formation after a gas bubble collapse near the micro fiber immersed in a liquid, Int J Heat Mass Transf 163 (2020), 120420, https://doi.org/10.1016/j.ijheatmasstransfer.2020.120420.
[41] Q. Yu, X. Ma, Z. Xu, J. Zhao, D. Wang, Z. Huang, Thermodynamic effect of single bubble near a rigid wall, Ultrason Sonochem 71 (2020) (2021), https://doi.org/10.1016/j.ultsonch.2020.105396.
[42] B. Liu, J. Cai, X. Huai, F. Li, Cavitation bubble collapse near a heated wall and its effect on the heat transfer, J Heat Transfer 136 (2) (2014) 1–7, https://doi.org/10.1115/1.4024071.
[43] S. Popinet, S. Zaleski, Bubble collapse near a solid boundary: A numerical study of the influence of viscosity, J Fluid Mech 464 (2002) 137–163, https://doi.org/10.1017/S002211200200856X.
[44] M. Brunhart, et al., Investigation of cavitation and vapor shedding mechanisms in a venturi nozzle, Phys. Fluids 32 (8) (2020) pp.
[45] E. Gomez Santos, J. Shi, M. Gavaises, C. Soteriou, M. Winterbourn, W. Bauer, Investigation of cavitation and air entrainment during pilot injection in real-size multi-hole diesel nozzles, Fuel 263 (Mar. 2020), 116746, https://doi.org/10.1016/J.FUEL.2019.116746.
[46] E. Gomez Santos, J. Shi, R. Venkatasubramanian, G. Hoffmann, M. Gavaises, W. Bauer, Modelling and prediction of cavitation erosion in GDi injectors

operated with E100 fuel, Fuel 289 (Apr. 2021), 119923, https://doi.org/10.1016/J.FUEL.2020.119923.
[47] Z. He, W. Guan, C. Wang, G. Guo, L. Zhang, M. Gavaises, Assessment of turbulence and cavitation models in prediction of vortex induced cavitating flow in fuel injector nozzles, Int. J. Multiph. Flow 157 (Dec. 2022), 104251, https://doi.org/10.1016/J.IJMULTIPHASEFLOW.2022.104251.
[48] M. Brunhart, C. Soteriou, C. Daveau, M. Gavaises, P. Koukouvinis, M. Winterbourn, Cavitation erosion risk indicators for a thin gap within a diesel fuel pump, Wear 442–443 (Feb. 2020), 203024, https://doi.org/10.1016/J.WEAR.2019.203024.
[49] M.-G. Mithun, P. Koukouvinis, M. Gavaises, Numerical simulation of cavitation and atomization using a fully compressible three-phase model, Phys Rev Fluids 3 (6) (2018) 64304.
[50] K. Kolovos, P. Koukouvinis, R.M. McDavid, M. Gavaises, Transient cavitation and friction-induced heating effects of diesel fuel during the needle valve early opening stages for discharge pressures up to 450 MPa, Energies (Basel) 14 (10) (2021) 2923.
[51] E. Stavropoulos Vasilakis, C. Rodriguez, N. Kyriazis, I. Malgarinos, P. Koukouvinis, M. Gavaises, A direct forcing immersed boundary method for cavitating flows, Int J Numer Methods Fluids 93 (10) (2021) 3092–3130.
[52] M. G. J. Vaz *et al.*, "Numerical Simulation of Multicomponent Diesel Fuel Spray Surrogates Using Real-Fluid Thermodynamic Modelling," 2022.
[53] M. Gavaises, M. Murali-Girija, C. Rodriguez, P. Koukouvinis, M. Gold, R. Pearson, Numerical simulation of fuel dribbling and nozzle wall wetting, Int. J. Engine Res. 23 (1) (2022) 132–149.
[54] A. Theodorakakos, G. Strotos, N. Mitroglou, C. Atkin, M. Gavaises, Friction-induced heating in nozzle hole micro-channels under extreme fuel pressurisation, Fuel 123 (May 2014) 143–150, https://doi.org/10.1016/J.FUEL.2014.01.050.
[55] G. Strotos, P. Koukouvinis, A. Theodorakakos, M. Gavaises, G. Bergeles, Transient heating effects in high pressure Diesel injector nozzles, Int J Heat Fluid Flow 51 (Feb. 2015) 257–267, https://doi.org/10.1016/J.IJHEATFLUIDFLOW.2014.10.010.
[56] P. Yi, S. Yang, C. Habchi, R. Lugo, A multicomponent real-fluid fully compressible four-equation model for two-phase flow with phase change, Phys. Fluids 31 (2019) 2.
[57] D. Fuster, A review of models for bubble clusters in cavitating flows, Flow Turbul Combust 102 (3) (Mar. 2019) 497–536, https://doi.org/10.1007/s10494-018-9993-4.
[58] N. Kyriazis, P. Koukouvinis, M. Gavaises, Modelling cavitation during drop impact on solid surfaces, Adv Colloid Interface Sci 260 (2018) 46–64.
[59] X. Ma, X. Zhao, B. Huang, X. Fu, and G. Wang, "Physical investigation of non-spherical bubble collapse near a rigid boundary," 2019.
[60] W. Wu, B. Wang, G. Xiang, Impingement of high-speed cylindrical droplets embedded with an air/vapour cavity on a rigid wall: numerical analysis, J Fluid Mech 864 (2019) 1058–1087, https://doi.org/10.1017/jfm.2019.55.
[61] T. Kondo, K. Ando, Simulation of high-speed droplet impact against a dry/wet rigid wall for understanding the mechanism of liquid jet cleaning, Phys. Fluids 31 (1) (2019) 13303.
[62] R. Dubois, E. Goncalves da Silva, P. Parnaudeau, High performance computing of stiff bubble collapse on CPU-GPU heterogeneous platform, Comput. Math. Appl. 99 (2021) 246–256, https://doi.org/10.1016/j.camwa.2021.07.010.
[63] T. Trummler, S.H. Bryngelson, K. Schmidmayer, S.J. Schmidt, T. Colonius, N. A. Adams, Near-surface dynamics of a gas bubble collapsing above a crevice, J Fluid Mech 899 (2020).
[64] E. Koukas, A. Papoutsakis, M. Gavaises, Numerical investigation of shock-induced bubble collapse dynamics and fluid–solid interactions during shock-wave lithotripsy, Ultrason Sonochem 95 (May 2023), 106393, https://doi.org/10.1016/J.ULTSONCH.2023.106393.
[65] A. Mishra, J. Mondal, A. Roy, R. Lakkaraju, P. Ghosh, Jet and shock characteristics of collapsing cavitating bubble in cryogenic environment, Indian Journal of Cryogenics 45 (1) (2020) 19–24, https://doi.org/10.5958/2349-2120.2020.00002.3.
[66] X. Ma et al. Numerical simulation of single bubble dynamics under acoustic travelling waves Ultrason Sonochem 42 December 2018 2017, pp. 619–630 10.1016/j.ultsonch.2017.12.021.
[67] S. Qiu, X. Ma, B. Huang, D. Li, G. Wang, M. Zhang, Numerical simulation of single bubble dynamics under acoustic standing waves, Ultrason Sonochem 49 (May) (2018) 196–205, https://doi.org/10.1016/j.ultsonch.2018.08.006.
[68] Q. Nguyen, V. Nguyen, T. Phan, T. Duy, S. Park, and W. Park, "Numerical study of dynamics of cavitation bubble collapse near oscillating walls Numerical study of dynamics of cavitation bubble collapse near oscillating walls," vol. 013306, no. January, 2023, doi: 10.1063/5.0132049.
[69] P. Koukouvinis, et al., Parametric investigations of the induced shear stress by a laser-generated bubble, Langmuir 34 (22) (2018) 6428–6442, https://doi.org/10.1021/acs.langmuir.8b01274.
[70] S. Y. Tong, S. P. Wang, S. Yan, and S. Li, "Fluid-structure interactions between a near-field underwater explosion bubble and a suspended plate," *AIP Adv*, vol. 12, no. 9, 2022, doi: 10.1063/5.0107299.
[71] A. Papoutsakis, P. Koukouvinis, M. Gavaises, Solution of cavitating compressible flows using Discontinuous Galerkin discretisation, J Comput Phys 410 (Jun. 2020), 109377, https://doi.org/10.1016/J.JCP.2020.109377.
[72] F. Denner, The Gilmore-NASG model to predict single-bubble cavitation in compressible liquids, Ultrason Sonochem 70 (May) (2021) 2020, https://doi.org/10.1016/j.ultsonch.2020.105307.
[73] A. Vidal, K. Kolovos, M.R. Gold, R.J. Pearson, P. Koukouvinis, M. Gavaises, Preferential cavitation and friction-induced heating of multi-component diesel fuel surrogates up to 450MPa, Int J Heat Mass Transf 166 (Feb. 2021), 120744, https://doi.org/10.1016/J.IJHEATMASSTRANSFER.2020.120744.
[74] N. Kyriazis, P. Koukouvinis, M. Gavaises, Numerical investigations on bubble-induced jetting and shock wave focusing: application on a needle-free injection, Proceedings of the Royal Society A 475 (2222) (2019), 20180548.
[75] M. Pelanti, K.M. Shyue, A mixture-energy-consistent six-equation two-phase numerical model for fluids with interfaces, cavitation and evaporation waves, J Comput Phys 259 (2014) 331–357, https://doi.org/10.1016/j.jcp.2013.12.003.
[76] R. Saurel and C. Pantano, "Diffuse-Interface Capturing Methods for Compressible Two-Phase Flows," *Phase Flows. Annual Review of Fluid Mechanics*, vol. 50, no. 1, pp. 105–130, 2018, [Online]. Available: https://hal.archives-ouvertes.fr/hal-02115896.
[77] I. Malgarinos, N. Nikolopoulos, M. Gavaises, Numerical investigation of heavy fuel droplet-particle collisions in the injection zone of a fluid catalytic cracking reactor, Part I: numerical model and 2D simulations, Fuel Process. Technol. 156 (Feb. 2017) 317–330, https://doi.org/10.1016/J.FUPROC.2016.09.014.
[78] C.W. Hirt, B.D. Nichols, Volume of fluid (VOF) method for the dynamics of free boundaries, J Comput Phys 39 (1) (1981) 201–225.
[79] I. Malgarinos, N. Nikolopoulos, M. Gavaises, Numerical investigation of heavy fuel droplet-particle collisions in the injection zone of a fluid catalytic cracking reactor, part II: 3D simulations, Fuel Process. Technol. 156 (Feb. 2017) 43–53, https://doi.org/10.1016/J.FUPROC.2016.09.012.
[80] P. Koukouvinis, M. Gavaises, O. Supponen, M. Farhat, Numerical simulation of a collapsing bubble subject to gravity, Phys. Fluids 28 (3) (2016) 32110.
[81] S. S. Jain, A. Mani, and P. Moin, "A conservative diffuse-interface method for compressible two-phase flows," *J Comput Phys*, p. 109606, 2020, doi: 10.1016/j.jcp.2020.109606.
[82] W. Wagner, A. Pruß, The IAPWS formulation 1995 for the thermodynamic properties of ordinary water substance for general and scientific use, J Phys Chem Ref Data 31 (2) (Jun. 2002) 387–535, https://doi.org/10.1063/1.1461829.
[83] J. Chandran, R.A. Salih, A modified equation of state for water for a wide range of pressure and the concept of water shock tube, Fluid Phase Equilib 483 (2019) 182–188, https://doi.org/10.1016/j.fluid.2018.11.032.
[84] M. Cismondi, J. Mollerup, Development and application of a three-parameter RK-PR equation of state, Fluid Phase Equilib 232 (1–2) (2005) 74–89, https://doi.org/10.1016/j.fluid.2005.03.020.
[85] S. Bidi, P. Koukouvinis, A. Papoutsakis, A. Shams, M. Gavaises, Numerical study of real gas effects during bubble collapse using a disequilibrium multiphase model, Ultrason Sonochem vol. 90, no. September (2022), 106175, https://doi.org/10.1016/j.ultsonch.2022.106175.
[86] W. Zhang, et al., AMReX: a framework for block-structured adaptive mesh refinement, J Open Source Softw 4 (37) (2019) 1370, https://doi.org/10.21105/joss.01370.
[87] N. Kyriazis, P. Koukouvinis, M. Gavaises, "Numerical investigation of bubble dynamics using tabulated data" 93 (2017) 158–177, https://doi.org/10.1016/j.ijmultiphaseflow.2017.04.004.
[88] M.J. Ivings, D.M. Causon, E.F. Toro, On Riemann solvers for compressible liquids, Int J Numer Methods Fluids 28 (3) (1998) 395–418, https://doi.org/10.1002/(SICI)1097-0363(19980915)28:3<395::AID-FLD718>3.0.CO;2-S.
[89] P.A. Thompson, G.S. Beavers, "Compressible-fluid dynamics" (1972).
[90] W. Wagner, H.-J. Kretzschmar, International Steam Tables-Properties of Water and Steam based on the Industrial Formulation IAPWS-IF97: Tables, Algorithms, Diagrams, and CD-ROM Electronic Steam Tables-All of the equations of IAPWS-IF97 including a complete set of supplementary backward, Springer Science & Business Media, 2007.
[91] D.E. Winterbone, A. Turan, "General thermodynamic relationships", in *advanced thermodynamics for engineers*, Elsevier (2015) 141–162, https://doi.org/10.1016/B978-0-444-63373-6.00007-1.
[92] H. Nazari-Mahroo, K. Pasandideh, H.A. Navid, R. Sadighi-Bonabi, Influence of liquid compressibility on the dynamics of single bubble sonoluminescence, Phys Lett A 382 (30) (Aug. 2018) 1962–1967, https://doi.org/10.1016/j.physleta.2018.04.058.
[93] P. Koukouvinis, M. Gavaises, O. Supponen, and M. Farhat, "Numerical simulation of a collapsing bubble subject to gravity," *Physics of Fluids*, vol. 28, no. 3, 2016, doi: 10.1063/1.4944561.
[94] Q. Zeng, S.R. Gonzalez-Avila, R. Dijkink, P. Koukouvinis, M. Gavaises, C.-D. Ohl, Wall shear stress from jetting cavitation bubbles, J Fluid Mech 846 (Jul. 2018) 341–355, https://doi.org/10.1017/jfm.2018.286.
[95] M. Koch, J.M. Rosselló, C. Lechner, W. Lauterborn, R. Mettin, Dynamics of a laser-induced bubble above the flat top of a solid cylinder—mushroom-shaped bubbles and the fast jet, Fluids 7 (1) (Dec. 2021) 2, https://doi.org/10.3390/fluids7010002.
[96] J.H. Dymond, R. Malhotra, The Tait equation: 100 years on, Int J Thermophys 9 (6) (1988) 941–951, https://doi.org/10.1007/BF01133262.
[97] A.H. Koop, Numerical simulation of unsteady three-dimensional sheet cavitation, University of Twente (2008).
[98] R. Saurel, J.P. Cocchi, P.B. Butler, Numerical study of cavitation in the wake of a hypervelocity underwater projectile, J Propuls Power 15 (4) (1999) 513–522, https://doi.org/10.2514/2.5473.
[99] E. Goncalves, Y. Hoarau, D. Zeidan, Simulation of shock-induced bubble collapse using a four-equation model, Shock Waves 29 (1) (Jan. 2019) 221–234, https://doi.org/10.1007/s00193-018-0809-1.
[100] J. Zhang, T.L. Jackson, A.M.D. Jost, Effects of air chemistry and stiffened EOS of air in numerical simulations of bubble collapse in water, Phys Rev Fluids 2 (5) (May 2017), 053603, https://doi.org/10.1103/PhysRevFluids.2.053603.

[101] T. Flatten, A. Morin, S.T. Munkejord, On solutions to equilibrium problems for systems of stiffened gases, SIAM J Appl Math 71 (1) (2011) 41–67, https://doi.org/10.1137/100784321.
[102] E.W. Lemmon, I.H. Bell, M.L. Huber, M.O. McLinden, "NIST Standard Reference Database 23: Reference Fluid Thermodynamic and Transport Properties-REFPROP, Version 10.0, National Institute of Standards and Technology", 2018.
[103] O. Le Métayer, R. Saurel, O. Le Métayer, R. Saurel, and T. N. Stiffened-gas, "The Noble-Abel Stiffened-Gas equation of state To cite this version : HAL Id : hal-01305974 The Noble-Abel Stiffened-Gas Equation of State," 2016.
[104] P. Koukouvinis, A. Vidal-Roncero, C. Rodriguez, M. Gavaises, L. Pickett, High pressure/high temperature multiphase simulations of dodecane injection to nitrogen: Application on ECN Spray-A, Fuel 275 (2020), 117871.
[105] M.R. Baer, J.W. Nunziato, A two-phase mixture theory for the deflagration-to-detonation transition (ddt) in reactive granular materials, Int. J. Multiph. Flow 12 (6) (1986) 861–889, https://doi.org/10.1016/0301-9322(86)90033-9.
[106] A. Chinnayya, E. Daniel, R. Saurel, Modelling detonation waves in heterogeneous energetic materials, J Comput Phys 196 (2) (2004) 490–538, https://doi.org/10.1016/j.jcp.2003.11.015.
[107] F. Richard Saurel, Petitpas, R.A. Berry, Simple and efficient relaxation methods for interfaces separating compressible fluids, cavitating flows and shocks in multiphase mixtures, J Comput Phys 228 (5) (2009) 1678–1712, https://doi.org/10.1016/j.jcp.2008.11.002.
[108] S. Le Martelot, R. Saurel, B. Nkonga, Towards the direct numerical simulation of nucleate boiling flows, Int. J. Multiph. Flow 66 (2014) 62–78, https://doi.org/10.1016/j.ijmultiphaseflow.2014.06.010.
[109] G. Allaire, S. Clerc, S. Kokh, A five-equation model for the simulation of interfaces between compressible fluids, J Comput Phys 181 (2) (2002) 577–616, https://doi.org/10.1006/jcph.2002.7143.
[110] A.B. Wood, R.B. Lindsay, A textbook of sound, Phys Today 9 (11) (1956) 37.
[111] G. Godounov, A. Sergueï Zabrodine, M. Ivanov, A. Kraiko, Prokopov,, Résolution numérique des problemes multidimensionnels de la dynamique des gaz, Editions Mir (1979), https://doi.org/10.18287/0134-2452-2015-39-4-459-461.
[112] B. Van Leer, Towards the ultimate conservative difference scheme III. Upstream-centered finite-difference schemes for ideal compressible flow, J Comput Phys 23 (3) (1977) 263–275, https://doi.org/10.1016/0021-9991(77)90094-8.
[113] E.F. Toro, Riemann solvers and numerical methods for fluid dynamics: a practical introduction, Springer Science & Business Media, 2013.
[114] W. Zhang, A. Myers, K. Gott, A. Almgren, J. Bell, AMReX: Block-structured adaptive mesh refinement for multiphysics applications, Int J High Perform Comput Appl 35 (6) (2021) 508–526.
[115] M.T. Henry de Frahan, et al., PeleC: An adaptive mesh refinement solver for compressible reacting flows, Int. J. High Perform. Comput. Appl. (2022), https://doi.org/10.1177/10943420221121151.
[116] J. Musser, et al., MFIX-Exa: A path toward exascale CFD-DEM simulations, Int. J. High Perform. Comput. Appl. 36 (1) (2022) 40–58, https://doi.org/10.1177/10943420211009293.
[117] M. Natarajan, R. Grout, W. Zhang, M. Day, A moving embedded boundary approach for the compressible Navier-Stokes equations in a block-structured adaptive refinement framework, J Comput Phys 465 (2022), 111315.
[118] C.E. Brennen, Cavitation and bubble dynamics. (2014), https://doi.org/10.1017/CBO9781107338760.
[119] D.L. Sokolov, M.R. Bailey, L.A. Crum, P.M. Blomgren, B.A. Connors, A.P. Evan, Prefocal alignment improves stone comminution in shockwave lithotripsy, J Endourol 16 (10) (2002) 709–715.
[120] E. Johnsen, T. Colonius, Shock-induced collapse of a gas bubble in shockwave lithotripsy, J Acoust Soc Am 124 (4) (2008) 2011–2020, https://doi.org/10.1121/1.2973229.
[121] A.R. Moritz, F.C. Henriques Jr, Studies of thermal injury: II. The relative importance of time and surface temperature in the causation of cutaneous burns, Am J Pathol 23 (5) (1947) 695.